# Fermi liquids beyond the forward-scattering limit: The role of nonforward scattering for scale invariance and instabilities

Han Ma [1] and Sung-Sik Lee [1,2]

[1] *Perimeter Institute for Theoretical Physics, Waterloo, Ontario, Canada N2L 2Y5*

[2] *Department of Physics & Astronomy, McMaster University, 1280 Main Street W, Hamilton, Ontario, Canada L8S 4M1*

(Received 14 April 2023; revised 14 September 2023; accepted 4 January 2024; published 23 January 2024)

Landau Fermi liquid theory is a fixed-point theory of metals that includes the forward-scattering amplitudes as exact marginal couplings. However, the fixed-point theory that only includes the strict forward scatterings is nonlocal in real space. In this paper, we revisit the Fermi liquid theory for charge-neutral fermions using the field-theoretic functional renormalization group formalism and show how the scale-invariant fixed point emerges as a local theory, which includes not only the forward scatterings but also nonforward scatterings with small but nonzero momentum transfers. In the low-energy limit, the near-forward scattering and pairing interactions take scale-invariant forms if the momentum transfer and the center-of-mass momentum of Cooper pairs, respectively, are comparable to the energy. The coupling functions fully capture the universal low-energy dynamics of the collective modes and instabilities of Fermi liquids. A runaway flow of the coupling function in the particle-hole channel beyond a critical interaction suggests an instability toward an ordered phase with a wave vector that depends on the interaction strength. At the critical interaction, the instability corresponds to the uniform Pomeranchuk or Stoner instability, but the momentum of the leading instability becomes nonzero for stronger attractive interaction. In the particle-particle channel, the coupling function reveals the dynamics of the unstable mode associated with the BCS instability. When an unstable normal metal evolves into the superconducting state, there exists a period in which a superconducting state with spatially nonuniform phase appears due to the presence of unstable Cooperon modes with nonzero momenta.

DOI: 10.1103/PhysRevB.109.045143

## I. INTRODUCTION

As one of the most prevalent phases of matter, metals and their phase transitions contain a rich physics that is central to our understanding of quantum materials. Thus the Landau Fermi liquid theory of metals has been one of the main pillars of modern condensed matter physics [1–4]. Introduced initially as a phenomenological model, it only keeps the strict forward-scattering amplitudes as interactions between quasiparticles. Despite its immediate success as a phenomenological theory, it took more than 30 years to theoretically justify the validity of the theory [5–10]. From the renormalization group (RG) point of view, Landau Fermi liquid theory represents a low-energy fixed point. Being a fixed-point theory valid strictly at zero energy, it is rightly nonlocal in real space at any finite length scale. On the other hand, it is desirable to have an effective field theory of Fermi liquids valid below a small but nonzero energy scale. Such an effective field theory must be local at length scales larger than the inverse of the energy scale. It will allow one to use the powerful machinery of local field theory in describing the emergence of Fermi liquids and their instabilities from a midinfrared energy scale down to the zero-energy limit. A complete understanding of Fermi liquids beyond the zero-energy limit is crucial for extracting scaling behaviors of physical observables at finite energies [11–14]. It will also serve as a solid reference point for theories of non-Fermi liquids [15–57]. For recent progress toward this goal that uses bosonization, see Refs. [58–60].

In this paper, we use the field-theoretic functional renormalization group scheme to describe Landau Fermi liquid and its instabilities within the framework of renormalizable local effective field theory [61]. The key ingredient of our work is the nonforward scatterings. A local effective field theory must include nonforward scatterings because, at any nonzero energy scale, fermions can exchange nonzero momenta while staying close to the Fermi surface within a thin energy shell. Let $\lambda^{\theta_1\theta_2}_{\theta_4\theta_3}$ represent the coupling function that describes the scattering of two low-energy fermions from angles $(\theta_4, \theta_3)$ to $(\theta_1, \theta_2)$ (Fig. 1). While Landau Fermi liquid theory only includes the strict forward-scattering amplitude $(\lambda^{\theta_1\theta_2}_{\theta_1\theta_2})$, the full coupling function does depend on $\theta_1 - \theta_4$ and $\theta_2 - \theta_3$ nontrivially. At a nonzero energy scale $\mu$, the coupling function changes smoothly but significantly as the differences in angles change by $\mu/k_F$, where $k_F$ is the Fermi momentum. If a UV theory is within the basin of attraction of the Fermi liquid fixed point, the coupling function flows to a scale-invariant form in the low-energy limit. The scale invariance becomes manifest once the transferred momentum is scaled along with the energy scale.

While the strict forward-scattering amplitude is exactly marginal [8], the nonforward-scattering amplitude does receive quantum corrections. The nontrivial RG flow of the general quartic coupling function can drive instabilities in particle-hole channels. If the UV theory has a sufficiently strong attractive interaction, the coupling function exhibits a runaway RG flow to the strong-coupling region due to the

 

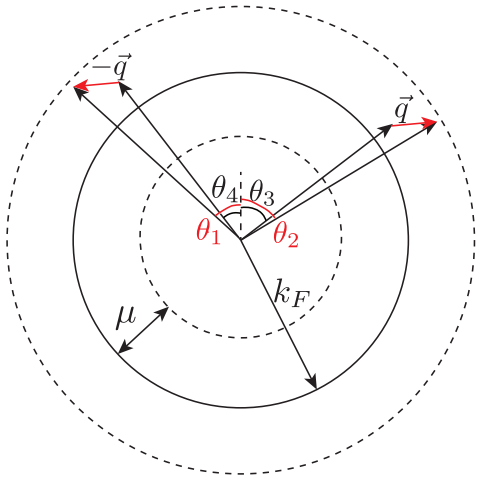


FIG. 1. At energy scale $\mu$, two fermions within the energy shell of thickness $\mu$ can undergo nonforward scatterings by exchanging small but nonzero momentum $\vec{q} \sim \mu$. General scattering processes are captured by coupling functions that depend on four angles. Alternatively, it can be viewed as a function of two angles for the incoming fermions and momentum transfer $\vec{q}$. At low energies, the coupling function acquires a nontrivial dependence on $\vec{q}/\mu$.

nontrivial renormalization of the nonforward scatterings. This implies that the general coupling function is a part of the low-energy data that should be kept within the low-energy effective theory with a small but nonzero energy cutoff. Within the local effective field theory, one should also consider general scattering processes in the particle-particle channel by including interactions of Cooper pairs with small but nonzero center-of-mass momenta. A scaling relation emerges in the general pairing interaction once the center-of-mass momentum is scaled along with the energy scale. In this paper, we focus on the charge-neutral Fermi liquids.

The rest of the paper is organized in the following way. In Sec. II, we introduce the local effective field theory for Fermi liquids. Section III discusses the effect of nonforward scattering in the near-forward-scattering channels. In Sec. III A, we present the scale-invariant coupling function that emerges at Fermi liquid fixed points. Section III B discusses the instability toward symmetry-broken states driven by the flow of nonforward-scattering amplitudes. The scaling behavior of the general pairing interaction is discussed in Sec. IV. In Sec. V, we discuss the experimental implications of the momentum-dependent coupling functions. We show that the coupling functions fully encode the universal low-energy dynamics of both stable and unstable collective modes of Fermi liquids. Besides reproducing known results on the zero-sound mode, we make predictions on instabilities in both particle-hole and particle-particle channels. Finally, Sec. VI summarizes the work.

## II. LOCAL EFFECTIVE FIELD THEORY

We consider a circular Fermi surface of spinful fermions that are subject to short-range interactions in two space dimensions. The following discussion can be generalized to higher dimensions in a straightforward way. The partition function is written as $Z = \int \mathcal{D}\psi^\dagger \mathcal{D}\psi\ e^{-S}$, and the action reads

$$\begin{aligned} S = &\sum_{\sigma=\pm} \int \frac{d\mathcal{V}_2}{(2\pi)^3}\, \psi^\dagger_\sigma(\omega,\vec{k})(-i\omega + \varepsilon_{\vec{k}})\psi_\sigma(\omega,\vec{k}) \\ &+ \frac{1}{4}\int \frac{d\mathcal{V}_4}{(2\pi)^9} \sum_{\sigma_{1,2,3,4}=\pm} (\lambda)^{\vec{k}+\frac{\vec{q}}{2},\sigma_1;\vec{p}-\frac{\vec{q}}{2},\sigma_2}_{\vec{k}-\frac{\vec{q}}{2},\sigma_4;\vec{p}+\frac{\vec{q}}{2},\sigma_3} \\ &\times\ \psi^\dagger_{\sigma_1}\left(\Omega+\frac{\omega}{2},\vec{k}+\frac{\vec{q}}{2}\right)\psi^\dagger_{\sigma_2}\left(\Omega'-\frac{\omega}{2},\vec{p}-\frac{\vec{q}}{2}\right) \\ &\times\ \psi_{\sigma_3}\left(\Omega'+\frac{\omega}{2},\vec{p}+\frac{\vec{q}}{2}\right)\psi_{\sigma_4}\left(\Omega-\frac{\omega}{2},\vec{k}-\frac{\vec{q}}{2}\right), \end{aligned} \tag{1}$$

where $d\mathcal{V}_2 = d\omega d^2\vec{k}$ and $d\mathcal{V}_4 = d\omega d\Omega d\Omega' d^2\vec{k}\, d^2\vec{p}\, d^2\vec{q}$ are the integral measures of the quadratic and quartic terms. $\psi_\sigma(\omega,\vec{k})$ denotes the fermionic field of spin $\sigma$, momentum $\vec{k}$, and frequency $\omega$. The bare dispersion is written as $\varepsilon_{\vec{k}} = \frac{1}{2m}(k^2 - k_F^2)$, where $k_F$ is the Fermi momentum. $\lambda$ is the four-fermion coupling, which is a function of momenta of the incoming and outgoing fermions.

At low energies, we focus on fermions that are close to the Fermi surface. In defining the low-energy scaling limit of the theory, it is convenient to use polar coordinates, where the two-dimensional momentum of a fermion is written as $\vec{k} = (k_F + \kappa)(\cos\theta, \sin\theta)$. $\kappa$ denotes the deviation of $|\vec{k}|$ from $k_F$, and $\theta$ is the polar angle. Accordingly, the fermion field is written as $\psi_{\sigma;\theta}(\omega,\kappa) \equiv \psi_\sigma(\omega,\vec{k})$. Low-energy effective field theories for a finite number of low-energy fields are characterized by a small number of coupling constants. In metals, Fermi surfaces support infinitely many gapless modes as the angle around the Fermi surface plays the role of a continuous flavor. Accordingly, the coupling constants are promoted to coupling functions that depend on angles. In the strict zero-energy limit, only two channels of interactions are allowed by the momentum conservation. The first is the forward scatterings, and the other is the pairing interactions. Those interactions involve pairs of fermions with zero center-of-mass momentum in the particle-hole and particle-particle channels, respectively. However, the interaction that only includes the strict forward scattering and the BCS interaction is nonlocal in the real space. At small but nonzero energies, the locality forces us to include interactions in which fermion pairs have small but nonzero center-of-mass momenta. This leads to the local low-energy effective action,

$$\begin{aligned} S = k_F \int \frac{d\bar{\mathcal{V}}_2}{(2\pi)^3} \sum_{\sigma=\pm} \psi^\dagger_{\sigma;\theta}(\omega,\kappa)(-i\omega + v_F\kappa)\psi_{\sigma;\theta}(\omega,\kappa) + \frac{k_F^2}{4}\int \frac{d\bar{\mathcal{V}}_4^{(0)}}{(2\pi)^9} \sum_{\sigma_{1,2,3,4}=\pm} (\lambda_0)^{\theta-\vartheta^S_\theta,\sigma_1;\ \theta'+\vartheta^S_{\theta'},\sigma_2}_{\theta+\vartheta^S_\theta,\sigma_4;\ \theta'-\vartheta^S_{\theta'},\sigma_3} \\ \times\ \psi^\dagger_{\sigma_1;\theta-\vartheta^S_\theta}\left[\Omega+\frac{\omega}{2},\kappa+k_F\vartheta^C_\theta\right]\psi^\dagger_{\sigma_2;\theta'+\vartheta^S_{\theta'}}\left[\Omega'-\frac{\omega}{2},\rho-k_F\vartheta^C_{\theta'}\right]\psi_{\sigma_3;\theta'-\vartheta^S_{\theta'}}\left[\Omega'+\frac{\omega}{2},\rho+k_F\vartheta^C_{\theta'}\right]\psi_{\sigma_4;\theta+\vartheta^S_\theta}\left[\Omega-\frac{\omega}{2},\kappa-k_F\vartheta^C_\theta\right] \end{aligned}$$

$$+\frac{k_F^2}{4}\int\frac{d\bar{\mathcal{V}}_4^{(1)}}{(2\pi)^9}\sum_{\sigma_{1,2,3,4}=\pm}(\lambda_1)^{\theta'-\varphi^S_{\theta'},\sigma_1;\,\theta'+\varphi^S_{\theta'}+\pi,\sigma_2}_{\theta-\varphi^S_\theta,\sigma_4;\,\theta+\varphi^S_\theta+\pi,\sigma_3}\psi^\dagger_{\sigma_1;\theta'-\varphi^S_{\theta'}}\Big[\Omega'+\frac{\omega}{2},\rho+k_F\varphi^C_{\theta'}\Big]\psi^\dagger_{\sigma_2;\theta'+\varphi^S_{\theta'}+\pi}\Big[-\Omega'+\frac{\omega}{2},\rho-k_F\varphi^C_{\theta'}\Big]$$
$$\times\,\psi_{\sigma_3;\theta+\varphi^S_\theta+\pi}\Big[-\Omega+\frac{\omega}{2},\kappa-k_F\varphi^C_\theta\Big]\psi_{\sigma_4;\theta-\varphi^S_\theta}\Big[\Omega+\frac{\omega}{2},\kappa+k_F\varphi^C_\theta\Big]. \tag{2}$$

Here, $d\bar{\mathcal{V}}_2=d\omega d\kappa d\theta$ denotes the integral measure associated with a unit length along the Fermi surface. The quartic interaction has been divided into the forward and BCS channels, whose integral measures are $d\bar{\mathcal{V}}_4^{(0)}=d\omega d\Omega d\Omega' dqqdkdpd\phi d\theta d\theta'$ and $d\bar{\mathcal{V}}_4^{(1)}=d\omega d\Omega d\Omega' dQQdkdpd\Phi d\theta d\theta'$, respectively. Here, $\lambda_0$ and $\lambda_1$ are the local coupling functions that include the forward and BCS scatterings [62]. They allow the total momenta of particle-hole and particle-particle pairs, denoted as $\vec{q}$ and $\vec{Q}$, respectively, to be nonzero. $\vec{q}$ and $\vec{Q}$ are also written in polar coordinates as $\vec{q}=q(\cos\phi,\sin\phi)$, $\vec{Q}=Q(\cos\Phi,\sin\Phi)$, where these momenta are not measured relative to the Fermi momentum unlike the momenta of fermions. In order for the fermions to stay close to the Fermi surface, the magnitudes of $\vec{q}$ and $\vec{Q}$ must to bounded by $\mu$ at energy scale $\mu$. However, it is crucial to allow the momentum transfer to be flexible within that range in order to keep the locality of the effective theory. $\vartheta^S_\theta=\frac{q}{2k_F}\sin(\theta-\phi)$ and $\varphi^S_\theta=\frac{Q}{2k_F}\sin(\theta-\Phi)$ denote the deviation of the angles away from the the strict forward-scattering and BCS-scattering channels, respectively. Similarly, $\vartheta^C_\theta=\frac{q}{2k_F}\cos(\theta-\phi)$ and $\varphi^C_\theta=\frac{Q}{2k_F}\cos(\theta-\Phi)$ determine the shift of the fermion energy caused by nonzero $q$ and $Q$ in the near-forward-scattering and BCS-scattering channels, respectively. The theory is specified by two parameters, $k_F$ and $v_F$, and two coupling functions, $\lambda_0$ and $\lambda_1$.

Under the scale transformation,

$$\begin{aligned}&\omega_s=\omega/s,\quad \Omega_s=\Omega/s,\quad \Omega'_s=\Omega'/s,\\ &\kappa_s=\kappa/s,\quad \rho_s=\rho/s,\quad q_s=q/s,\\ &Q_s=Q/s,\quad \psi_{s;\sigma;\theta}(\omega_s,\kappa_s)=s^2\psi_{\sigma;\theta}(\omega,\kappa),\end{aligned} \tag{3}$$

which leaves angles unchanged, the coupling constants ($v_F$, $k_F$) and coupling functions ($\lambda_0$, $\lambda_1$) are transformed as

$$\begin{aligned}&k_{s;F}=k_F/s,\quad v_{s;F}=v_F,\\ &\vartheta^A_{s;\theta}=\frac{q_s}{2k_{s;F}}\mathbb{A}(\theta-\phi)=\vartheta^A_\theta,\\ &\varphi^A_{s;\theta}=\frac{Q_s}{2k_{s;F}}\mathbb{A}(\theta-\Phi)=\varphi^A_\theta,\end{aligned} \tag{4}$$

with $A=S,C$ and $\mathbb{A}=\sin,\cos$

$$(\lambda_{s;0})^{\theta-\vartheta^S_\theta,\sigma_1;\theta'+\vartheta^S_{\theta'},\sigma_2}_{\theta+\vartheta^S_\theta,\sigma_4;\theta'-\vartheta^S_{\theta'},\sigma_3}=s(\lambda_0)^{\theta-\vartheta^S_\theta,\sigma_1;\theta'+\vartheta^S_{\theta'},\sigma_2}_{\theta+\vartheta^S_\theta,\sigma_4;\theta'-\vartheta^S_{\theta'},\sigma_3},$$
$$(\lambda_{s;1})^{\theta'-\varphi^S_{s,\theta'},\sigma_1;\theta'+\varphi^S_{s,\theta'}+\pi,\sigma_2}_{\theta-\varphi^S_{s,\theta},\sigma_4;\theta+\varphi^S_{s,\theta}+\pi,\sigma_3}=s(\lambda_1)^{\theta'-\varphi^S_{\theta'},\sigma_1;\theta'+\varphi^S_{\theta'}+\pi,\sigma_2}_{\theta-\varphi^S_\theta,\sigma_4;\theta+\varphi^S_\theta+\pi,\sigma_3}.$$

A few comments on the tree-level scaling are in order. First, the four-fermion couplings have scaling dimension $-1$. Nonetheless, the low-energy effective field theory must include them because they can give rise to infrared (IR) singularity. In metals, the degree of IR singularity that a coupling can create does not necessarily match its scaling dimension because of the scale associated with the Fermi momentum. Consequently, the notion of renormalizable field theory needs to be generalized for metals [61]. Second, $k_F$ has scaling dimension 1 and runs toward infinity in the low-energy ($s\to 0$) limit. This is because the size of the Fermi surface measured in the unit of the floating energy scale increases as the low-energy limit is taken. Here, $k_F$ plays the role of a metric that controls the "proper" size of the Fermi surface [63]. Third, the action has scaling dimension 1 rather than 0 under this scale transformation [64]. This is an unusual choice in that action is regarded as dimensionless in most field theories. However, this is natural for theories with continuously many gapless modes where the manifold that supports gapless modes comes with a momentum scale. The fact that the low-energy effective action has a positive dimension reflects the fact that the number of patches connected by nonforward scattering increases with decreasing energy [65]. At low energies, the magnitude of typical momentum transfer $\vec{q}$ in the nonforward scattering decreases, which makes the number of decoupled patches increase at low energies.

Now, we consider quantum corrections that renormalize the couplings. We first define the couplings in terms of physical observables. $k_F$ does not receive quantum corrections due to Luttinger's theorem. $v_F$ and the coupling functions are defined through the two-point and the four-point vertex functions through

$$\begin{aligned}&\frac{\partial}{\partial\kappa}\mathrm{Re}\Gamma_{(2)}(k^*)=v_F+F_1,\\ &i\frac{\partial}{\partial\omega}\mathrm{Im}\Gamma_{(2)}(k^*)=1+F_2,\end{aligned} \tag{5}$$
$$(\Gamma_{(4)})^{k_1^*,\sigma_1;k_2^*,\sigma_2}_{k_4^*,\sigma_4;k_3^*,\sigma_3}=(\lambda_0)^{\theta-\vartheta^S_\theta,\sigma_1;\theta'+\vartheta^S_{\theta'},\sigma_2}_{\theta+\vartheta^S_\theta,\sigma_4;\theta'-\vartheta^S_{\theta'},\sigma_3}+F_3, \tag{6}$$
$$(\Gamma_{(4)})^{p_1^*,\sigma_1;p_2^*,\sigma_2}_{p_4^*,\sigma_4;p_3^*,\sigma_3}=(\lambda_1)^{\theta'-\varphi^S_{\theta'},\sigma_1;\theta'+\varphi^S_{\theta'}+\pi,\sigma_2}_{\theta-\varphi^S_\theta,\sigma_4;\theta+\varphi^S_\theta+\pi,\sigma_3}+F_4. \tag{7}$$

Here, $\Gamma_{(2)}$ and $\Gamma_{(4)}$ represent the two-point and four-point vertex functions, respectively. The energy-momentum vectors used to impose the RG condition are chosen to be

$$k^*=(\mu,k_F\cos\theta,k_F\sin\theta),\quad k_1^*=\Big(3\mu,k_F\cos\theta+\frac{q}{2}\cos\phi,k_F\sin\theta+\frac{q}{2}\sin\phi\Big),$$
$$k_2^*=\Big(-\mu,k_F\cos\theta'-\frac{q}{2}\cos\phi,k_F\sin\theta'-\frac{q}{2}\sin\phi\Big),\quad k_3^*=\Big(\mu,k_F\cos\theta'+\frac{q}{2}\cos\phi,k_F\sin\theta'+\frac{q}{2}\sin\phi\Big),$$

$$k_4^* = \Big(\mu, k_F\cos\theta - \frac{q}{2}\cos\phi, k_F\sin\theta - \frac{q}{2}\sin\phi\Big), \quad p_1^* = \Big(3\mu, k_F\cos\theta' + \frac{Q}{2}\cos\Phi, k_F\sin\theta' + \frac{Q}{2}\sin\Phi\Big),$$
$$p_2^* = \Big(-\mu, -k_F\cos\theta' + \frac{Q}{2}\cos\Phi, -k_F\sin\theta' + \frac{Q}{2}\sin\Phi\Big), \quad p_3^* = \Big(\mu, -k_F\cos\theta + \frac{Q}{2}\cos\Phi, -k_F\sin\theta + \frac{Q}{2}\sin\Phi\Big),$$
and $$p_4^* = \Big(\mu, k_F\cos\theta + \frac{Q}{2}\cos\Phi, k_F\sin\theta + \frac{Q}{2}\sin\Phi\Big).$$

The frequencies, which are of the order of the floating energy scale $\mu$, are chosen such that infrared divergences are cut off by $\mu$ in all particle-particle and particle-hole channels. The spatial momenta lie on the Fermi surface when $\vec{q}$ and $\vec{Q}$ vanish. $F_i$ are RG-scheme-dependent corrections that are regular in the small $\mu$ limit. The local counterterms needed to enforce the RG conditions are written as

$$\begin{aligned}
S_{\rm CT} =& k_F\int\frac{d\bar{\mathcal{V}}_2}{(2\pi)^3}\sum_{\sigma=\pm}\psi^\dagger_{\sigma;\theta}(\omega,\kappa)(-i\delta_1\omega+\delta_2 v_F\kappa)\psi_{\sigma;\theta}(\omega,\kappa) + \frac{k_F^2}{4}\int\frac{d\bar{\mathcal{V}}_4^{(0)}}{(2\pi)^9}\sum_{\sigma_{1,2,3,4}=\pm}\big(A_0^\lambda\lambda_0\big)^{\theta-\vartheta^S_\theta,\sigma_1;\ \theta'+\vartheta^S_{\theta'},\sigma_2}_{\theta+\vartheta^S_\theta,\sigma_4;\ \theta'-\vartheta^S_{\theta'},\sigma_3}\psi^\dagger_{\sigma_1;\theta-\vartheta^S_\theta}\\
&\times\Big[\Omega+\frac{\omega}{2},\kappa+k_F\vartheta^C_\theta\Big]\psi^\dagger_{\sigma_2;\theta'+\vartheta^S_{\theta'}}\Big[\Omega'-\frac{\omega}{2},\rho-k_F\vartheta^C_{\theta'}\Big]\psi_{\sigma_3;\theta'-\vartheta^S_{\theta'}}\Big[\Omega'+\frac{\omega}{2},\rho+k_F\vartheta^C_{\theta'}\Big]\psi_{\sigma_4;\theta+\vartheta^S_\theta}\Big[\Omega-\frac{\omega}{2},\kappa-k_F\vartheta^C_\theta\Big]\\
&+\frac{k_F^2}{4}\int\frac{d\bar{\mathcal{V}}_4^{(1)}}{(2\pi)^9}\sum_{\sigma_{1,2,3,4}=\pm}\big(A_1^\lambda\lambda_1\big)^{\theta'-\varphi^S_{\theta'},\sigma_1;\ \theta'+\varphi^S_{\theta'}+\pi,\sigma_2}_{\theta-\varphi^S_\theta,\sigma_4;\ \theta+\varphi^S_\theta+\pi,\sigma_3}\psi^\dagger_{\sigma_1;\theta'-\varphi^S_{\theta'}}\Big[\Omega'+\frac{\omega}{2},\rho+k_F\varphi^C_{\theta'}\Big]\psi^\dagger_{\sigma_2;\theta'+\varphi^S_{\theta'}+\pi}\Big[-\Omega'+\frac{\omega}{2},\rho-k_F\varphi^C_{\theta'}\Big]\\
&\times\psi_{\sigma_3;\theta+\varphi^S_\theta+\pi}\Big[-\Omega+\frac{\omega}{2},\kappa-k_F\varphi^C_\theta\Big]\psi_{\sigma_4;\theta-\varphi^S_\theta}\Big[\Omega+\frac{\omega}{2},\kappa+k_F\varphi^C_\theta\Big].
\end{aligned}\tag{8}$$

Because the effective field theory is local, the RG condition can be enforced with local counterterms. The bare action becomes

$$\begin{aligned}
S_B =& k_{F;B}\int\frac{d\bar{\mathcal{V}}_{2;B}}{(2\pi)^3}\sum_{\sigma=\pm}\psi^\dagger_{B;\sigma;\theta}(\omega_B,\kappa)(-i\omega_B+v_F\kappa)\psi_{B;\sigma;\theta}(\omega_B,\kappa) + \frac{k_{F;B}^2}{4}\int\frac{d\bar{\mathcal{V}}_{4;B}^{(0)}}{(2\pi)^9}\sum_{\sigma_{1,2,3,4}=\pm}(\lambda_{0;B})^{\theta-\vartheta^S_{\theta;B},\sigma_1;\ \theta'+\vartheta^S_{\theta';B},\sigma_2}_{\theta+\vartheta^S_{\theta;B},\sigma_4;\ \theta'-\vartheta^S_{\theta';B},\sigma_3}\\
&\times\psi^\dagger_{B;\sigma_1;\theta-\vartheta^S_{\theta;B}}\Big[\Omega_B+\frac{\omega_B}{2},\kappa+k_F\vartheta^C_{\theta;B}\Big]\psi^\dagger_{B;\sigma_2;\theta'+\vartheta^S_{\theta';B}}\Big[\Omega'_B-\frac{\omega_B}{2},\rho-k_F\vartheta^C_{\theta';B}\Big]\psi_{B;\sigma_3;\theta'-\vartheta^S_{\theta';B}}\Big[\Omega'_B+\frac{\omega_B}{2},\rho+k_F\vartheta^C_{\theta';B}\Big]\\
&\times\psi_{B;\sigma_4;\theta+\vartheta^S_{\theta;B}}\Big[\Omega_B-\frac{\omega_B}{2},\kappa-k_F\vartheta^C_{\theta;B}\Big] + \frac{k_{F;B}^2}{4}\int\frac{d\bar{\mathcal{V}}_{4;B}^{(1)}}{(2\pi)^9}\sum_{\sigma_{1,2,3,4}=\pm}(\lambda_{1;B})^{\theta'-\varphi^S_{\theta';B},\sigma_1;\ \theta'+\varphi^S_{\theta';B}+\pi,\sigma_2}_{\theta-\varphi^S_{\theta;B},\sigma_4;\ \theta+\varphi^S_{\theta;B}+\pi,\sigma_3}\\
&\times\psi^\dagger_{B;\sigma_1;\theta'-\varphi^S_{\theta';B}}\Big[\Omega'_B+\frac{\omega_B}{2},\rho+k_F\varphi^C_{\theta';B}\Big]\psi^\dagger_{B;\sigma_2;\theta'+\varphi^S_{\theta';B}+\pi}\Big[-\Omega'_B+\frac{\omega_B}{2},\rho-k_F\varphi^C_{\theta';B}\Big]\\
&\times\psi_{B;\sigma_3;\theta+\varphi^S_{\theta;B}+\pi}\Big[-\Omega_B+\frac{\omega_B}{2},\kappa-k_F\varphi^C_{\theta;B}\Big]\psi_{B;\sigma_4;\theta-\varphi^S_{\theta;B}}\Big[\Omega_B+\frac{\omega_B}{2},\kappa+k_F\varphi^C_{\theta;B}\Big].
\end{aligned}\tag{9}$$

The bare variables [66] are related to the renormalized variables through the multiplicative renormalization factors, $Z_i = 1+\delta_i$, $(Z_i^\lambda)^{\theta_1,\theta_2}_{\theta_4,\theta_3} = 1 + (A_i^\lambda)^{\theta_1,\theta_2}_{\theta_4,\theta_3}$ for $i = 1, 2$,

$$\begin{aligned}
\omega_B &= \frac{Z_1}{Z_2}\omega, \quad \psi_B = \sqrt{\frac{Z_2^2}{Z_1}}\psi,\\
(\lambda_{i;B})^{\theta_1,\theta_2}_{\theta_4,\theta_3} &= \frac{(Z_i^\lambda)^{\theta_1,\theta_2}_{\theta_4,\theta_3}\mu^{-1}(\tilde{\lambda}_i)^{\theta_1,\theta_2}_{\theta_4,\theta_3}}{Z_1Z_2},\\
k_{B;F} &= \mu\tilde{k}_F.
\end{aligned}\tag{10}$$

Here, we use the scheme in which $v_F$ is fixed. $(\tilde{\lambda}_i)^{\theta_1,\theta_2}_{\theta_4,\theta_3} = \mu(\lambda_i)^{\theta_1,\theta_2}_{\theta_4,\theta_3}$ and $\tilde{k}_F = \mu^{-1}k_F$ represent dimensionless objects that are measured in units of the floating energy scale. The beta functionals for the coupling functions are obtained by keeping $\lambda_{i;B}$ fixed while varying the floating energy. This leads to the beta functionals

$$\frac{d(\tilde{\lambda}_i)^{\theta_1,\theta_2}_{\theta_4,\theta_3}}{dl} = \left[-1-3(z-1)-4\eta_\psi+\frac{d\ln\big(Z_i^\lambda\big)^{\theta_1,\theta_2}_{\theta_4,\theta_3}}{d\ln\mu}\right]\times(\tilde{\lambda}_i)^{\theta_1,\theta_2}_{\theta_4,\theta_3}.\tag{11}$$

Here $l = \ln(\Lambda/\mu)$ is the logarithmic length scale with $\Lambda$ being a UV cutoff. $z = \frac{d\ln Z_1/Z_2}{d\ln\mu}$ is the dynamical critical exponent, and $\eta_\psi = \frac{d\ln\sqrt{Z_2^2/Z_1}}{d\ln\mu}$ is the anomalous dimension of the fermion. The dimensionless Fermi momentum obeys $\frac{d\tilde{k}_F}{dl} = \tilde{k}_F$.

At the one-loop order, only the following diagrams contribute to the beta functionals:

$\Gamma^{(4)} =$ 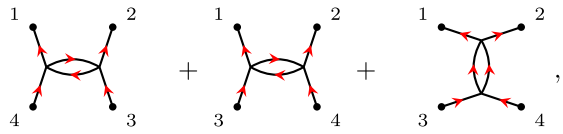 , (12)

$z = 1$ and $\eta_\psi = 0$. The first diagram contributes to the near-forward scatterings. The third diagram contributes the pairing interaction. In the following sections, we compute the beta functionals in the two channels for general $\vec{q}$ and $\vec{Q}$.

## III. NEARLY FORWARD SCATTERING

At the one-loop order, only the first diagram in Eq. (12) contributes to the quantum correction of the near-forward-scattering processes. The counterterm reads

$$\begin{aligned}
&\left(A_0^{\lambda}\lambda_0\right)^{\theta-\vartheta_\theta^S,\sigma_1;\theta'+\vartheta_{\theta'}^S,\sigma_2}_{\theta+\vartheta_\theta^S,\sigma_4;\theta'-\vartheta_{\theta'}^S,\sigma_3} \\
&\quad = -\frac{1}{2\mu}\frac{k_F}{\mu}\int\frac{d\theta''d\kappa''}{(2\pi)^2}\frac{d\Omega''}{2\pi}\sum_{\sigma',\sigma''}(\tilde{\lambda}_0)^{\theta-\vartheta_\theta^S,\sigma_1;\theta''+\vartheta_{\theta''}^S,\sigma''}_{\theta+\vartheta_\theta^S,\sigma_4;\theta''-\vartheta_{\theta''}^S,\sigma'} \\
&\qquad \times (\tilde{\lambda}_0)^{\theta''-\vartheta_{\theta''}^S,\sigma';\theta'+\vartheta_{\theta'}^S,\sigma_2}_{\theta''+\vartheta_{\theta''}^S,\sigma'';\theta'-\vartheta_{\theta'}^S,\sigma_3} \\
&\qquad \times \mathrm{Re}\left[\frac{1}{-i\Omega''+v_F\left[\kappa''-\frac{q}{2}\cos(\theta''-\phi)\right]}\right. \\
&\qquad \left.\times\frac{1}{-i(\mu+\Omega'')+v_F\left[\kappa''+\frac{q}{2}\cos(\theta''-\phi)\right]}\right].
\end{aligned} \tag{13}$$

The integrations over $\kappa''$ and $\Omega''$ can be readily performed. Apart from the overall factor of $1/\mu$ determined from the dimension of the quartic coupling, the counterterm is proportional to $k_F/\mu$. This reflects the fact that the phase space of the virtual particle-hole pairs is proportional to $k_F$. The phase space measured in the unit $\mu$ increases with decreasing $\mu$. This extensive phase space is what promotes the quartic coupling to the marginal coupling although it has scaling dimension $-1$ [61]. One can incorporate the phase space to define a new dimensionless coupling function as $[F_{\theta,\theta'}(q,\phi)]^{\sigma_1;\sigma_2}_{\sigma_4;\sigma_3} = \frac{k_F}{\mu}(\tilde{\lambda}_0)^{\theta-\vartheta_\theta^S,\sigma_1;\theta'+\vartheta_{\theta'}^S,\sigma_2}_{\theta+\vartheta_\theta^S,\sigma_4;\theta'-\vartheta_{\theta'}^S,\sigma_3}$. The beta functional for $F$ becomes independent of $k_F$,

$$\begin{aligned}
\frac{dF^r_{\theta_1,\theta_2}(q,\phi)}{dl} &= -\frac{1}{4\pi^2 v_F}\int_0^{2\pi}d\theta\; F^r_{\theta_1,\theta}(q,\phi)F^r_{\theta,\theta_2}(q,\phi) \\
&\quad\times\frac{\mu^2 v_F^2 q^2\cos^2(\theta-\phi)}{\left[\mu^2+v_F^2q^2\cos^2(\theta-\phi)\right]^2}.
\end{aligned} \tag{14}$$

Here, $r = s$ or $a$. $F^s_{\theta_1,\theta_2}(q,\phi)$ and $F^a_{\theta_1,\theta_2}(q,\phi)$ represent the projections of $[F_{\theta,\theta'}(q,\phi)]^{\sigma_1;\sigma_2}_{\sigma_4;\sigma_3}$ to the singlet and adjoint representations of a particle-hole pair for the SU(2) group, respectively,

$$[F_{\theta_1,\theta_2}]^{\sigma_1;\sigma_2}_{\sigma_4;\sigma_3} = \mathfrak{S}^{\sigma_1,\sigma_2}_{\sigma_4,\sigma_3}F^s_{\theta_1,\theta_2} + \mathfrak{A}^{\sigma_1,\sigma_2}_{\sigma_4,\sigma_3}F^a_{\theta_1,\theta_2}, \tag{15}$$

where $\mathfrak{S}^{\sigma_1,\sigma_2}_{\sigma_4,\sigma_3} = \frac{1}{2}\delta^{\sigma_1}_{\sigma_4}\delta^{\sigma_2}_{\sigma_3}$ and $\mathfrak{A}^{\sigma_1,\sigma_2}_{\sigma_4,\sigma_3} = \delta^{\sigma_1}_{\sigma_3}\delta^{\sigma_2}_{\sigma_4} - \frac{1}{2}\delta^{\sigma_1}_{\sigma_4}\delta^{\sigma_2}_{\sigma_3}$. From now on, we omit the superscript $r$ because the following analysis holds for both channels. Note that the kernel in Eq. (14) is the contribution of the one-loop particle-hole bubble that renormalizes the vertex function [3].

The beta functional in Eq. (14) vanishes at $q = 0$ for any nonzero $\mu$. This is consistent with the fact that the strict forward-scattering amplitude is exactly marginal. However, for any nonzero $\mu$, the beta functional is nontrivial for $q \neq 0$. This has interesting consequences. First, when the theory flows to a fixed point in the low-energy limit, the full coupling function of the local effective field theory exhibits a scale invariance when the momentum transfer is comparable to the energy scale. Second, the nontrivial renormalization group flow of the nonforward-scattering amplitude can create instabilities if the bare coupling is sufficiently negative. In the following, we discuss these consequences in detail.

For a fixed momentum transfer, we can view the coupling $F$ as a matrix of two angles that play the role of continuous indices. Here, the product of two matrices is given by $(\mathbf{A}\cdot\mathbf{B})_{\theta_1,\theta_2} = \int\frac{d\theta}{2\pi}\mathbf{A}_{\theta_1\theta}\mathbf{B}_{\theta\theta_1}$, and $\mathbf{M}^{-1}$ denotes the inverse of matrix $\mathbf{M}$. Then, Eq. (14) can be cast into $\frac{d\mathbf{F}}{dl} = -\mathbf{F}\cdot\mathbf{D}\cdot\mathbf{F}$, where $\mathbf{D}_{\theta,\theta'} = -\frac{1}{v_F}\frac{\mu^2v_F^2q^2\cos^2(\theta-\phi)}{[\mu^2+v_F^2q^2\cos^2(\theta-\phi)]^2}\delta(\theta-\theta')$. Multiplying $\mathbf{F}^{-1}$ on both sides of Eq. (14), we obtain

$$\frac{d[\mathbf{F}(q,\phi)]^{-1}_{\theta,\theta'}}{dl} = \frac{\delta(\theta-\theta')}{v_F}\frac{\mu^2v_F^2q^2\cos^2(\theta-\phi)}{\left[\mu^2+v_F^2q^2\cos^2(\theta-\phi)\right]^2}. \tag{16}$$

At scale $\mu$, the beta functional is largest for $q\cos(\theta-\phi)\sim\mu$. For $\theta-\phi\sim\pi/2$, the phase space of $q$ is largest because virtual particle-hole pairs with momentum $\vec{q}$ cost the least energy in the region of the Fermi surface where $\vec{q}$ is tangential to the Fermi surface. The solution of Eq. (16) is given by

$$\begin{aligned}
&[\mathbf{F}(q,\phi;\mu)]^{-1}_{\theta,\theta'} \\
&\quad = \frac{\delta(\theta-\theta')}{2v_F}\left[\frac{v_F^2q^2\cos^2(\theta-\phi)}{\mu^2+v_F^2q^2\cos^2(\theta-\phi)}\right. \\
&\qquad \left.-\frac{v_F^2q^2\cos^2(\theta-\phi)}{\Lambda^2+v_F^2q^2\cos^2(\theta-\phi)}\right] + [\mathbf{F}(q,\phi;\Lambda)]^{-1}_{\theta,\theta'},
\end{aligned} \tag{17}$$

where $\mathbf{F}(q,\phi;\Lambda)$ is the coupling function at the UV cutoff, $\Lambda$. One can combine the last two terms to define the coupling function at $\mu=\infty$ to simplify the solution as

$$\begin{aligned}
[\mathbf{F}(q,\phi;\mu)]^{-1}_{\theta,\theta'} &= \frac{1}{2v_F}\delta(\theta-\theta')\frac{v_F^2q^2\cos^2(\theta-\phi)}{\mu^2+v_F^2q^2\cos^2(\theta-\phi)} \\
&\quad + [\mathbf{F}(q,\phi;\infty)]^{-1}_{\theta,\theta'}.
\end{aligned} \tag{18}$$

### A. Scale invariance of Fermi liquid fixed points

Let us first consider the case in which no eigenvalue of $\mathbf{F}$ diverges at any $\mu$. In this case, the theory is expected to flow to a Fermi liquid fixed point in the low-energy limit if the interaction is repulsive in the pairing channel. It is noted that the $\mu\to0$ limit and the $q\to0$ limit do not commute. In the strict forward-scattering limit ($q=0$), the coupling function does not depend on $\mu$ at all. On the other hand, if one takes the $\mu\to0$ limit for a fixed $q\neq0$, the coupling function saturates to $[\mathbf{F}(q,\phi;0)]^{-1}_{\theta,\theta'} = \frac{1}{8\pi^2v_F}\delta(\theta-\theta') + [\mathbf{F}(q,\phi;\infty)]^{-1}_{\theta,\theta'}$

in the low-energy limit. The nontrivial crossover between these two limits can be captured by the scale-invariant coupling function defined by $[\tilde{\mathbf{F}}(\tilde{q},\phi;\mu)]_{\theta,\theta'} \equiv [\mathbf{F}(\mu\tilde{q},\phi;\mu)]_{\theta,\theta'}$, where $\tilde{q} = q/\mu$ corresponds to the dimensionless momentum transfer measured in units of $\mu$. This allows us to probe the kinematic region with small but nonzero momentum transfers. By taking the $\mu \to 0$ limit with fixed $\tilde{q}$, the coupling function becomes

$$\lim_{\mu\to 0}[\tilde{\mathbf{F}}(\tilde{q},\phi;\mu)]^{-1}_{\theta,\theta'} = \frac{\delta(\theta-\theta')}{2v_F}\frac{v_F^2\tilde{q}^2\cos^2(\theta-\phi)}{1+v_F^2\tilde{q}^2\cos^2(\theta-\phi)} + [\mathbf{F}(0,0;\infty)]^{-1}_{\theta,\theta'}. \tag{19}$$

Here, we use the fact that $[\mathbf{F}(q,\phi;\infty)]_{\theta,\theta'}$ is an analytic function of $\vec{q}$. In the $\mu \to 0$ limit, only $[\mathbf{F}(q=0,\phi=0;\infty)]_{\theta,\theta'}$ enters in the expression for the fixed-point coupling function. Equation (19) corresponds to the fixed point of a beta functional, $\frac{d[\tilde{\mathbf{F}}(\tilde{q},\phi)]_{\theta,\theta'}}{d\ell}|_{\tilde{q},\theta,\theta'} = \frac{d[\mathbf{F}(q,\phi)]_{\theta,\theta'}}{d\ell}|_{q,\theta,\theta'} - \tilde{q}\frac{\partial[\tilde{\mathbf{F}}(\tilde{q},\phi)]_{\theta,\theta'}}{\partial\tilde{q}}$, where the second term in the new beta functional corresponds to a momentum dilatation that "magnifies" the region with small momentum transfers as the low-energy limit is taken. It is noted that the scale-invariant coupling function obeys the $z = 1$ scaling. The momentum transfer and energy scale in the same way because the energy of a particle-hole pair with momentum $\vec{q} = q(\cos\phi, \sin\phi)$ created near the Fermi surface at angle $\theta$ scales linearly in $q$ as far as $\theta - \phi \neq \pi/2$. Equation (19) is the central result of our paper. The local coupling function captures the full extent of the scale-invariant Fermi liquid fixed point away from the strict forward-scattering limit. As expected, the only UV information that is kept in the fixed-point coupling is the forward-scattering amplitude at $\vec{q} = 0$.

In general, it is not easy to invert Eq. (19) to write down $[\tilde{\mathbf{F}}(\tilde{q},\phi;\mu)]_{\theta,\theta'}$ in a closed form [67]. If the UV coupling function is nonzero only in one angular momentum channel, the coupling function in the IR limit can be easily obtained. To see this, we start by writing Eq. (17) in the space of angular momentum,

$$[\mathbf{F}(q,\phi;\mu)]^{-1}_{\ell,\ell'} = \int\frac{d\theta\, e^{i(\ell-\ell')\theta}}{8\pi^2 v_F} \times\left[\frac{v_F^2q^2\cos^2(\theta-\phi)}{\mu^2+v_F^2q^2\cos^2(\theta-\phi)} - \frac{v_F^2q^2\cos^2(\theta-\phi)}{\Lambda^2+v_F^2q^2\cos^2(\theta-\phi)}\right] + [\mathbf{F}(q,\phi;\Lambda)]^{-1}_{\ell,\ell'}, \tag{20}$$

where $\ell$ and $\ell'$ are conjugate momenta associated with $\theta$ and $\theta'$, respectively, and $\mathbf{M}_{\ell,\ell'} = \int\frac{d\theta d\theta'}{(2\pi)^2}\mathbf{M}_{\theta,\theta'}e^{i(\ell\theta-\ell'\theta')}$. In the angular momentum basis, the fixed-point coupling function can be written as

$$\mathbf{F}(q,\phi;\mu) = [\mathbf{F}(q,\phi;\Lambda)]([\boldsymbol{\mathcal{D}}'(q,\phi;\mu,\Lambda) \times \mathbf{F}(q,\phi;\Lambda)] + I)^{-1}, \tag{21}$$

where $\boldsymbol{\mathcal{D}}'_{\ell,\ell'}(q,\phi;\mu,\Lambda) = e^{i(\ell-\ell')\phi}\mathcal{D}_{\ell,\ell'}(q;\mu,\Lambda)$ with $\mathcal{D}_{\ell,\ell'}(q;\mu,\Lambda) = [D_{\ell-\ell'}(q;\mu) - D_{\ell-\ell'}(q;\Lambda)]$ and

$$D_{\ell-\ell'}(q;\mu) = \int\frac{d\theta\, e^{i\theta(\ell-\ell')}}{8\pi^2 v_F}\frac{v_F^2q^2\cos^2(\theta)}{\mu^2+v_F^2q^2\cos^2(\theta)}. \tag{22}$$

$D_\ell(q,\mu)$ vanishes for odd $\ell$. For $\ell = 0, 2, 4$, it takes the form of

$$D_0(q;\mu) = \frac{1}{4\pi v_F}\left[1-\frac{1}{\sqrt{1+\frac{v_F^2q^2}{\mu^2}}}\right],$$

$$D_2(q;\mu) = \frac{1}{4\pi v_F}\frac{\mu^2}{v_F^2q^2}\left[\sqrt{1+\frac{v_F^2q^2}{\mu^2}}+\frac{1}{\sqrt{1+\frac{v_F^2q^2}{\mu^2}}}-2\right],$$

$$D_4(q;\mu) = \frac{1}{4\pi v_F}\left[4\left(1+\frac{2\mu^2}{v_F^2q^2}-\frac{2\mu}{v_Fq}\sqrt{\frac{\mu^2}{v_F^2q^2}+1}\right) - \frac{\mu}{v_Fq}\frac{1}{\sqrt{\frac{\mu^2}{v_F^2q^2}+1}}\right]. \tag{23}$$

### *1. s wave*

Let us first consider the case where the forward-scattering amplitude of the UV coupling is independent of angles, $[\mathbf{F}(q,\phi;\Lambda)]_{\theta,\theta'} = \alpha$, where $\alpha$ denotes the strength of the coupling in the $s$-wave channel. In the basis of angular momentum, the UV coupling is written as $[\mathbf{F}(q,\phi;\Lambda)]_{\ell,\ell'} = \alpha\delta_{\ell,0}\delta_{\ell',0}$. Using $[\boldsymbol{\mathcal{D}}'(q,\phi;\mu,\Lambda)\mathbf{F}(q,\phi;\Lambda)]_{\ell,\ell'} = \alpha\mathcal{D}'_{\ell,0}(q,\phi;\mu,\Lambda)\delta_{\ell',0}$, we can write $\boldsymbol{\mathcal{D}}'(q,\phi;\mu,\Lambda)\mathbf{F}(q,\phi;\Lambda)+I$ as

$$\boldsymbol{\mathcal{D}}'(q,\phi;\mu,\Lambda)\mathbf{F}(q,\phi;\Lambda)+I = \begin{bmatrix} 1 & 0 & \alpha\mathcal{D}'_{-2}(q,\phi;\mu,\Lambda) & 0 & 0\\ 0 & 1 & 0 & 0 & 0\\ 0 & 0 & 1+\alpha\mathcal{D}'_0(q,\phi;\mu,\Lambda) & 0 & 0\\ 0 & 0 & 0 & 1 & 0\\ 0 & 0 & \alpha\mathcal{D}'_2(q,\phi;\mu,\Lambda) & 0 & 1\end{bmatrix}, \tag{24}$$

where the matrix elements are explicitly shown only in the $5\times 5$ block of $-2 \leqslant \ell, \ell' \leqslant 2$. This leads to the isotropic IR quartic coupling function, $\mathbf{F}(q,\phi;\mu) = \mathbf{F}(q,\phi;\Lambda)[\boldsymbol{\mathcal{D}}'(q,\phi;\mu,\Lambda)\mathbf{F}(q,\phi;\Lambda)+I]^{-1} = \delta_{\ell,0}\delta_{\ell',0}F(q,\phi;\mu)$, where $F(q,\phi;\mu) = \frac{\alpha}{\alpha\mathcal{D}_{0,0}(q;\mu,\Lambda)+1} = \alpha\{\frac{\alpha}{4\pi v_F}[\frac{1}{\sqrt{1+\frac{v_F^2q^2}{\Lambda^2}}}-\frac{1}{\sqrt{1+\frac{v_F^2q^2}{\mu^2}}}]+1\}^{-1}$. In the space of angles, we readily obtain

$$[\mathbf{F}(q,\phi;\mu)]_{\theta,\theta'} = \frac{\alpha}{\frac{\alpha}{4\pi v_F}\left[\frac{1}{\sqrt{1+\frac{v_F^2q^2}{\Lambda^2}}}-\frac{1}{\sqrt{1+\frac{v_F^2q^2}{\mu^2}}}\right]+1}. \tag{25}$$

In the large $\Lambda$ limit, it takes a simpler form,

$$F(q,\phi;\mu) = \alpha\left\{\frac{\alpha}{4\pi v_F}\left[1-\frac{1}{\sqrt{1+\frac{v_F^2q^2}{\mu^2}}}\right]+1\right\}^{-1}. \tag{26}$$

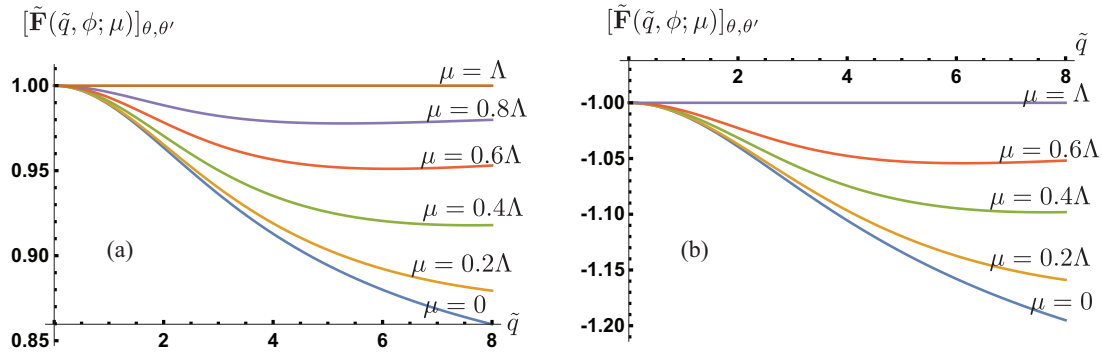


FIG. 2. RG flow of $[\tilde{\mathbf{F}}(\tilde{q},\phi;\mu)]_{\theta,\theta'}$ for a momentum-independent UV coupling function $[\mathbf{F}(q,\phi;\Lambda)]_{\theta,\theta'}=\alpha$ with (a) $\alpha=1$ and (b) $\alpha=-1$. For both plots, we choose $v_F=0.3$ and $\Lambda=10$. For the angle-independent UV coupling function, $[\tilde{\mathbf{F}}(\tilde{q},\phi;\mu)]_{\theta,\theta'}$ remains independent of $\phi$, $\theta$, and $\theta'$ at all scales. The coupling function in the $\mu\to 0$ limit represents the fixed-point profile.

Figure 2 shows the evolution of coupling functions. In the low-energy limit, the coupling function converges to the fixed-point profile,

$$[\tilde{\mathbf{F}}(\tilde{q},\phi;0)]_{\theta,\theta'}=\frac{\alpha}{\frac{\alpha}{4\pi v_F}\left[1-\frac{1}{\sqrt{1+v_F^2\tilde{q}^2}}\right]+1}. \tag{27}$$

#### 2. *d* wave

As the next example, let us consider the case where the UV coupling has only the $d$-wave component, $[\mathbf{F}(q,\phi;\Lambda)]_{\theta,\theta'}=2\alpha\cos[2(\theta-\theta')]$. In the angular momentum basis, the UV coupling function can be written as $[\mathbf{F}(q,\phi;\Lambda)]_{\ell,\ell'}=\alpha(\delta_{\ell,-2}\delta_{\ell',-2}+\delta_{\ell,2}\delta_{\ell',2})$. From

$$\sum_{l''}\boldsymbol{\mathcal{D}}'_{\ell,\ell''}(q,\phi;\mu,\Lambda)[\mathbf{F}(q,\phi;\Lambda)]_{\ell'',\ell'}=\alpha[\boldsymbol{\mathcal{D}}'_{\ell,-2}(q,\phi;\mu,\Lambda)\delta_{\ell',-2}+\boldsymbol{\mathcal{D}}'_{\ell,2}(q,\phi;\mu,\Lambda)\delta_{\ell',2}], \tag{28}$$

we obtain the 5×5 block of $\boldsymbol{\mathcal{D}}'(q,\phi;\mu,\Lambda)\mathbf{F}(q,\phi;\Lambda)+I$ for $-2\leqslant\ell,\ell'\leqslant 2$ as

$$\boldsymbol{\mathcal{D}}'(q,\phi;\mu,\Lambda)\mathbf{F}(q,\phi;\Lambda)+I=\begin{bmatrix}1+\alpha\mathcal{D}'_0(q,\phi;\mu,\Lambda) & 0 & 0 & 0 & \alpha\mathcal{D}'_{-4}(q,\phi;\mu,\Lambda)\\ 0 & 1 & 0 & 0 & 0\\ \alpha\mathcal{D}'_2(q,\phi;\mu,\Lambda) & 0 & 1 & 0 & \alpha\mathcal{D}'_{-2}(q,\phi;\mu,\Lambda)\\ 0 & 0 & 0 & 1 & 0\\ \alpha\mathcal{D}'_4(q,\phi;\mu,\Lambda) & 0 & 0 & 0 & 1+\alpha\mathcal{D}'_0(q,\phi;\mu,\Lambda)\end{bmatrix}. \tag{29}$$

The nonzero components of the IR coupling function and its expression in the angle basis are

$$[\mathbf{F}(q,\phi;\mu)]_{\ell,\ell'}=\alpha\frac{[1+\alpha\mathcal{D}_0(q;\mu,\Lambda)](\delta_{\ell,2}\delta_{\ell',2}+\delta_{\ell,-2}\delta_{\ell,-2})-\alpha\mathcal{D}_4(q;\mu,\Lambda)(e^{4i\phi}\delta_{\ell,2}\delta_{\ell',-2}+e^{-4i\phi}\delta_{\ell,-2}\delta_{\ell',2})}{1+2\alpha\mathcal{D}_0(q;\mu,\Lambda)+\alpha^2\left[\mathcal{D}_0^2(q;\mu,\Lambda)-\mathcal{D}_4^2(q;\mu,\Lambda)\right]}, \tag{30}$$

$$[\mathbf{F}(q,\phi;\mu)]_{\theta,\theta'}=2\alpha\frac{[1+\alpha\mathcal{D}_0(q;\mu,\Lambda)]\cos[2(\theta-\theta')]-\alpha\mathcal{D}_4(q;\mu,\Lambda)\cos[2(\theta+\theta')-4\phi]}{1+2\alpha\mathcal{D}_0(q;\mu,\Lambda)+\alpha^2\left[\mathcal{D}_0^2(q;\mu,\Lambda)-\mathcal{D}_4^2(q;\mu,\Lambda)\right]}. \tag{31}$$

In the $\mu\to 0$ limit, with $\tilde{q}=q/\mu$ and

$$\tilde{D}_0(x)=\frac{1}{4\pi v_F}\left[1-\frac{1}{\sqrt{1+v_F^2x^2}}\right],\quad \tilde{D}_4(x)=\frac{1}{4\pi v_F}\left[-\frac{1}{\sqrt{1+v_F^2x^2}}+\frac{4}{v_F^2x^2}\left(1+\frac{2}{v_F^2x^2}-\frac{2}{v_Fx}\sqrt{1+\frac{1}{v_F^2x^2}}\right)\right], \tag{32}$$

the coupling function takes the universal form given by

$$[\tilde{\mathbf{F}}(\tilde{q},\phi;0)]_{\theta,\theta'}=\left\{1+2\alpha\tilde{D}_0(\tilde{q})+\alpha^2\left[\tilde{D}_0^2(\tilde{q})-\tilde{D}_4^2(\tilde{q})\right]\right\}^{-1}2\alpha\left\{\left[1+\alpha\tilde{D}_0(\tilde{q})\right]\cos[2(\theta-\theta')]-\alpha\tilde{D}_4(\tilde{q})\cos[2(\theta+\theta')-4\phi]\right\}. \tag{33}$$

The evolution of the coupling function is shown in Fig. 3. In Fig. 4, the coupling function is shown as a function of angle at different energy scales.

### B. Instabilities of Fermi liquids in the particle-hole channel

So far, we have considered the cases where the theory flows to the Fermi liquid fixed point in the low-energy limit.

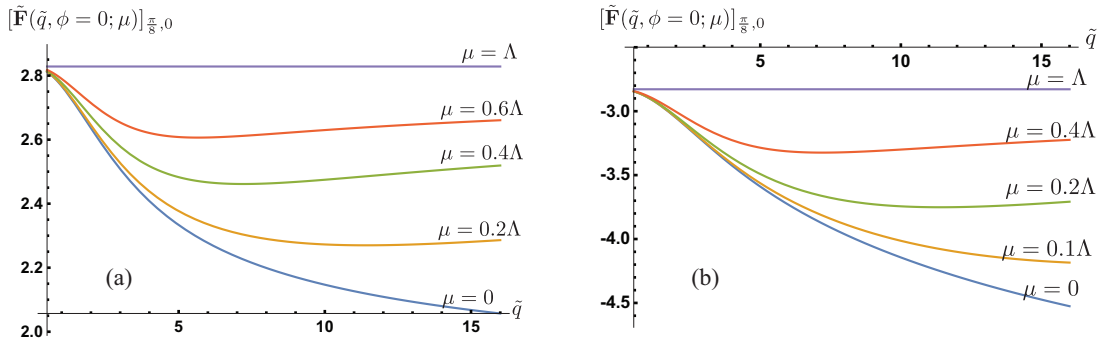


FIG. 3. RG flow of $[\tilde{\mathbf{F}}(\tilde{q},\phi=0;\mu)]_{\frac{\pi}{8},0}$ for a $d$-wave UV coupling function $[\mathbf{F}(q,\phi;\Lambda)]_{\theta,\theta'}=2\alpha\cos[2(\theta-\theta')]$ for (a) $\alpha=2$ and (b) $\alpha=-2$. We use $v_F=0.3$ and $\Lambda=10$.

If the UV coupling is sufficiently attractive in one or more angular momentum channels, some eigenvalues of the coupling function can diverge at low energies, signifying potential instabilities. However, this instability in the particle-hole channel requires a finite strength of coupling. While the perturbative analysis is not expected to be quantitatively valid, the main point of this analysis is to highlight the importance of quantum corrections to nonforward scatterings for particle-hole instabilities.

### *1. The s-wave channel*

Let us first consider the angle-independent UV coupling function, $[\mathbf{F}(q,\phi;\Lambda)]_{\theta,\theta'}=\alpha$. For $\alpha>-4\pi v_F$, eigenvalues of the coupling function remain finite at all energy scales. The coupling function that emerges in the $\mu\to 0$ limit represents the scale-invariant Fermi liquid fixed point. The renormalization group flow changes qualitatively for sufficiently attractive interaction with $\alpha\leqslant -4\pi v_F$. For $\alpha\leqslant -4\pi v_F$, the coupling function at nonzero momenta can diverge at low energies. As $\mu$ is lowered, the divergence arises first at the momentum where the energy of the particle-hole pair peaks. This is because the quantum correction in the particle-hole channel vanishes in the strict forward-scattering limit and increases with increasing energy of the particle-hole pair. The precise momentum at which the divergence arises at the highest energy depends on the full band structure. To be concrete, here we consider the simple case where the particle-hole energy dispersion is well approximated by the linear dispersion before it peaks at $q_c$ and bends down at larger momenta. In this case, Eq. (17) holds up to $q\sim q_c$, and the coupling function diverges at $q=q_c$ as $\mu$ approaches a critical energy scale $\mu_c$. The divergence of the four-fermion coupling at a nonzero $q$ can potentially represent a charge or spin density wave instability, depending on whether the divergence is in the spin-singlet or spin-triplet channel [68]. If the divergence arises at $q_c\gg\mu_c$, however, one needs to be careful in interpreting it as a sign of instability because the low-energy effective theory description is not valid at $q$ larger than $\mu$. With this cautionary remark, we show the evolution of coupling in the deep attractive region in Fig. 5. In Fig. 6, we show the evolution of $[\tilde{\mathbf{F}}(\tilde{q},\phi;\mu_c)]_{\theta,\theta'}$ as the strength of the UV coupling is tuned.

### *2. The d-wave channel*

Next, let us consider the case where the UV coupling is attractive in the $d$-wave channel with $[\mathbf{F}(q,\phi;\infty)]_{\theta,\theta'}=2\alpha\cos[2(\theta-\theta')]$. In Fig. 7, we plot the evolution of $[\mathbf{F}(q,\phi=0;\mu)]_{\frac{\pi}{8},0}$ as $\mu$ is lowered. For $\alpha\leqslant\alpha_c=-4\pi v_F$, the coupling function at $q=q_c$ diverges as a critical energy scale $\mu_c$ is approached. Figure 8 shows the angular dependence of $[\mathbf{F}(q_c,\phi=0;\mu)]_{\theta,0}$ at different $\mu/\Lambda$. A large attractive interaction for particle-hole pairs in the $d$-wave channel with a nonzero momentum promotes a distortion of the Fermi surface with a spatial modulation. This corresponds to a bond density wave that causes a spatial modulation in the pattern of rotational symmetry breaking.

Figure 9 shows the profile of the coupling function that emerges in the $\mu\to\mu_c$ limit from the UV coupling function $[\mathbf{F}(q,\phi;\Lambda)]_{\theta,\theta'}=2\alpha\cos[2(\theta-\theta')]$ for different values of $\alpha$. Figure 10 shows how $[\mathbf{F}(q,\phi=0;\mu_c)]_{\theta,0}$ evolves as $\alpha$

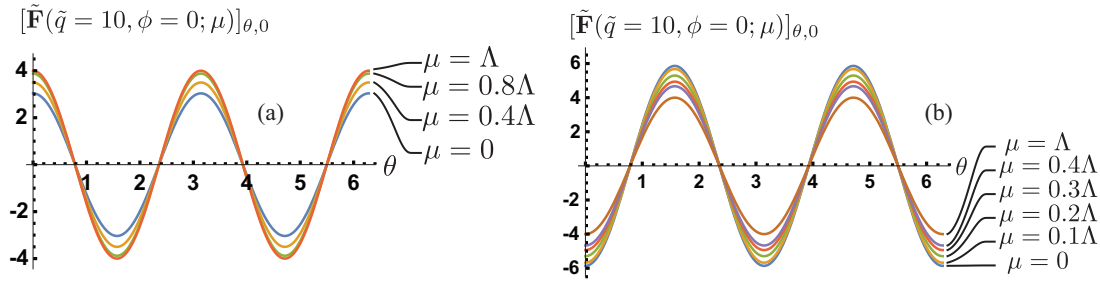


FIG. 4. $[\tilde{\mathbf{F}}(\tilde{q}=10,\phi=0;\mu)]_{\theta,0}$ plotted as a function of $\theta$ at different values of $\mu$ for (a) $\alpha=2$ and (b) $\alpha=-2$. The same UV coupling function and parameters are used as in Fig. 3.

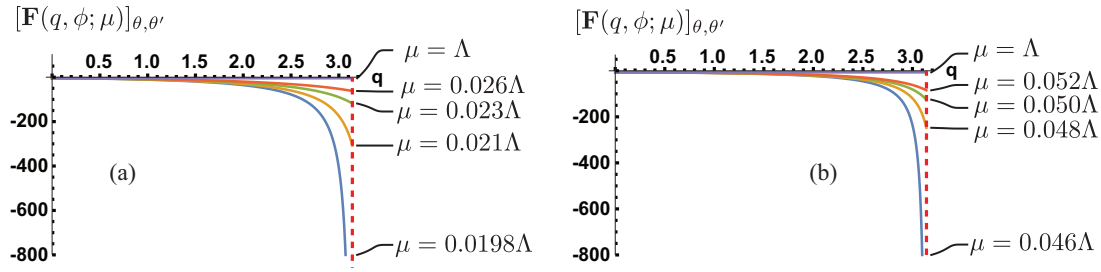


FIG. 5. RG flow of $[\mathbf{F}(q,\phi;\mu)]_{\theta,\theta'}$ for an attractive UV coupling function $[\mathbf{F}(q,\phi;\Lambda)]_{\theta,\theta'}=\alpha$ with (a) $\alpha=-(4\pi v_F+1)$ and (b) $\alpha=-(4\pi v_F+3)$. The coupling function diverges at the momentum cutoff, which is chosen to be $q_c=\pi$, at $\mu_c=0.0198\Lambda$ and $\mu_c=0.046\Lambda$, respectively. We use $\Lambda=10$ and $v_F=0.3$.

is varied. For $\alpha>\alpha_c$, the coupling function converges to a fixed profile in the low-energy limit. On the other hand, the amplitude of the coupling function grows without a bound as $\mu$ approaches $\mu_c$ for $\alpha\leqslant\alpha_c$.

## IV. PAIRING CHANNEL

In this section, we discuss the renormalization group flow for the general pairing interaction that includes Cooper pairs with nonzero center-of-mass momentum. The counterterm from the one-loop vertex correction reads

$$(A_1^{\lambda}\lambda_1)^{\theta'-\varphi^S_{\theta'},\sigma_1;\theta'+\varphi^S_{\theta'}+\pi,\sigma_2}_{\theta-\varphi^S_{\theta},\sigma_4;\theta+\varphi^S_{\theta}+\pi,\sigma_3}=\frac{1}{2\mu}\frac{k_F}{\mu}\int\frac{d\theta''d\kappa''}{(2\pi)^2}\frac{d\Omega''}{2\pi}\sum_{\sigma',\sigma''}(\tilde{\lambda}_1)^{\theta'-\varphi^S_{\theta'},\sigma_1;\theta'+\varphi^S_{\theta'}+\pi,\sigma_2}_{\theta''-\varphi^S_{\theta''},\sigma';\theta''+\varphi^S_{\theta''}+\pi,\sigma''}(\tilde{\lambda}_1)^{\theta''-\varphi^S_{\theta''},\sigma';\theta''+\varphi^S_{\theta''}+\pi,\sigma''}_{\theta-\varphi^S_{\theta},\sigma_4;\theta+\varphi^S_{\theta}+\pi,\sigma_3}$$
$$\times\,\mathrm{Re}\left[\frac{1}{-i\Omega''+\frac{1}{2m}\left[2k_F\kappa''+(\kappa'')^2+(k_F+\kappa'')Q\cos(\theta''-\Phi)+\frac{Q^2}{4}\right]}\right.$$
$$\left.\times\,\frac{1}{-i(\mu-\Omega'')+\frac{1}{2m}\left[2k_F\kappa''+(\kappa'')^2-(k_F+\kappa'')Q\cos(\theta''-\Phi)+\frac{Q^2}{4}\right]}\right]. \tag{34}$$

The factor of $k_F/\mu$ represents the extensive phase space available for virtual Cooper pairs in the loop. We define a dimensionless coupling function that incorporates the phase space as $[V_{\theta',\theta}(Q,\Phi)]^{\sigma_1,\sigma_2}_{\sigma_4,\sigma_3}\equiv\frac{k_F}{\mu}(\tilde{\lambda}_1)^{\theta'-\varphi^S_{\theta'},\sigma_1;\theta'+\varphi^S_{\theta'}+\pi,\sigma_2}_{\theta-\varphi^S_{\theta},\sigma_4;\theta+\varphi^S_{\theta}+\pi,\sigma_3}$. The beta functional for this new coupling is given by

$$\frac{dV^r_{\theta_1,\theta_2}(Q,\Phi)}{dl}=-\frac{1}{8\pi^2 v_F}\int d\theta\; V^r_{\theta_1,\theta}(Q,\Phi)V^r_{\theta,\theta_2}(Q,\Phi)\left[\frac{\mu^2}{\mu^2+v_F^2Q^2\cos^2(\theta-\Phi)}\right]. \tag{35}$$

Here, $r=+$ or $-$. $V^+_{\theta_1,\theta_2}(Q,\Phi)$ and $V^-_{\theta_1,\theta_2}(Q,\Phi)$ represent the pairing interactions in the spin-triplet and spin-singlet channels, respectively,

$$[V_{\theta',\theta}]^{\sigma_1,\sigma_2}_{\sigma_4,\sigma_3}=\mathcal{S}^{\sigma_1,\sigma_2}_{\sigma_4,\sigma_3}V^+_{\theta_1,\theta_2}+\mathcal{A}^{\sigma_1,\sigma_2}_{\sigma_4,\sigma_3}V^-_{\theta_1,\theta_2}, \tag{36}$$

where $\mathcal{S}^{\sigma_1,\sigma_2}_{\sigma_4,\sigma_3}=\frac{1}{2}(\delta^{\sigma_1}_{\sigma_3}\delta^{\sigma_2}_{\sigma_4}+\delta^{\sigma_1}_{\sigma_4}\delta^{\sigma_2}_{\sigma_3})$ and $\mathcal{A}^{\sigma_1,\sigma_2}_{\sigma_4,\sigma_3}=\frac{1}{2}(\delta^{\sigma_1}_{\sigma_4}\delta^{\sigma_2}_{\sigma_3}-\delta^{\sigma_1}_{\sigma_3}\delta^{\sigma_2}_{\sigma_4})$. From now on, we focus on one spin channel and omit the superscript $r$ in $V$. For Cooper pairs with zero center-of-mass momentum, we set $Q=0$ to reproduce the well-known beta functional [8], $\frac{dV_{\theta_1,\theta_2}(0,0)}{dl}=-\frac{1}{8\pi^2 v_F}\int d\theta V_{\theta_1,\theta}(0,0)V_{\theta,\theta_2}(0,0)$.

For general $Q$, the solution of the beta functional is written as

$$[\mathbf{V}(Q,\Phi;\mu)]^{-1}_{\theta,\theta'}=\frac{\delta(\theta-\theta')}{4v_F}\ln\left[\frac{\Lambda^2+v_F^2Q^2\cos^2(\theta-\Phi)}{\mu^2+v_F^2Q^2\cos^2(\theta-\Phi)}\right]+[\mathbf{V}(Q,\Phi;\Lambda)]^{-1}_{\theta,\theta'}, \tag{37}$$

where $[\mathbf{V}(Q,\Phi;\Lambda)]_{\theta,\theta'}$ denotes the pairing interaction at UV cutoff $\Lambda$. The most important aspect of Eq. (37) is the logarithmic singularity that is present at $Q=0$ and $\mu=0$. If $[\mathbf{V}(Q,\Phi;\Lambda)]_{\theta,\theta'}$ is repulsive in all angular momentum channels, the coupling function flows to zero logarithmically. On the other hand, the coupling function at $Q=0$ diverges at a critical energy scale if $[\mathbf{V}(Q,\Phi;\Lambda)]_{\theta,\theta'}$ has any channel with a negative eigenvalue. This is the well-known BCS instability. Here, we focus on the scaling behavior of the coupling function at nonzero $Q$. To remove the logarithmic divergence, we consider the difference of Eq. (37) at two momenta, $Q$ and $Q_*$. In the $\mu\to0$ limit with fixed $\tilde{Q}=Q/\mu$ and $\tilde{Q}_*=Q_*/\mu$, the difference becomes

$$\lim_{\mu\to0}\left([\tilde{\mathbf{V}}(\tilde{Q},\Phi;\mu)]^{-1}_{\theta,\theta'}-[\tilde{\mathbf{V}}(\tilde{Q}_*,\Phi;\mu)]^{-1}_{\theta,\theta'}\right)=\frac{\delta(\theta-\theta')}{4v_F}\ln\left[\frac{1+v_F^2\tilde{Q}_*^2\cos^2(\theta-\Phi)}{1+v_F^2\tilde{Q}^2\cos^2(\theta-\Phi)}\right], \tag{38}$$

where $[\tilde{\mathbf{V}}(\tilde{Q},\Phi;\mu)]_{\theta,\theta'}=[\mathbf{V}(\mu\tilde{Q},\Phi;\mu)]_{\theta,\theta'}$.

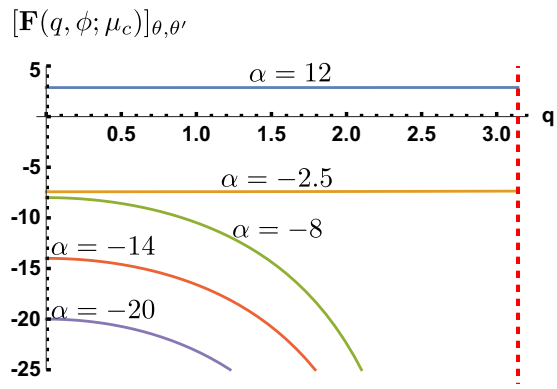


FIG. 6. The profile of the coupling function that emerges in the $\mu \to \mu_c$ limit from the UV coupling function $[\mathbf{F}(q,\phi;\Lambda)]_{\theta,\theta'} = \alpha$ for different values of $\alpha$. For stable Fermi liquids, with $\alpha > -4\pi v_F\sqrt{1+v_F^2\frac{q^2}{\Lambda^2}}$, $\mu_c = 0$. For unstable cases, the critical energy scales are given by $\mu_c = 0.580$, $\mu_c = 0.995$, and $\mu_c = 1.288$ for $\alpha = -8$, $\alpha = -14$, and $\alpha = -20$, respectively, for the choice of $v_F = 0.3$ and $\Lambda = 10$.

Now, let us consider a simple case where the UV coupling function is nonzero only in the $s$-wave spin-singlet channel. The beta functional for the coupling in the $s$-wave channel becomes

$$\frac{dV_0(Q;\mu)}{dl} = -\frac{V_0^2(Q;\mu)}{8\pi^2 v_F}\int d\theta\ \frac{\mu^2}{\mu^2 + v_F^2 Q^2\cos^2(\theta)}, \quad (39)$$

where $V_0$ represents the coupling in the $s$-wave channel. The solution is written as

$$[V_0(Q;\mu)]^{-1} = \frac{1}{4\pi v_F}\ln\left[\frac{\sqrt{v_F^2Q^2+\Lambda^2}+\Lambda}{\sqrt{v_F^2Q^2+\mu^2}+\mu}\right] + [V_0(Q;\Lambda)]^{-1}, \quad (40)$$

where $V_0(Q;\Lambda)$ is the $s$-wave coupling defined at UV cutoff scale $\Lambda$. In Fig. 11, we plot the evolution of the coupling functions for different choices of the UV coupling in the $s$-wave channel. In this example, the scale invariance is expressed as

$$\lim_{\mu\to 0}[\tilde{V}_0(\tilde{Q};\mu)]^{-1} = [\tilde{V}_0(\tilde{Q}_*)]^{-1} + \frac{1}{4\pi v_F}\ln\left[\frac{\sqrt{v_F^2\tilde{Q}_*^2+1}+1}{\sqrt{v_F^2\tilde{Q}^2+1}+1}\right] \quad (41)$$

in the $\mu \to 0$ limit with fixed $\tilde{Q}$ and $\tilde{Q}_*$.

## V. EXPERIMENTAL CONSEQUENCES

In this section, we discuss how the universal coupling functions manifest themselves in physical observables. In particular, we show that our local effective field theory contains all dynamical information for low-energy collective modes. This is in contrast to the fact that Landau's fixed-point theory and the earlier RG schemes that do not keep track of the universal momentum dependence of the coupling functions cannot capture the collective modes and one has to resort to more microscopic theories to describe them. Below, we examine the bosonic collective modes with charge 0 and 2, respectively. The main result of this section is that we can identify the collective modes of Fermi liquids from the poles of the coupling functions in the space of frequency. Because this section is somewhat long, we begin with a brief summary of the key results.

In the particle-hole channel, Fig. 12 shows the poles of the coupling functions in the space of frequency for various choices of UV coupling. For the system with repulsive interactions, the poles represent well-defined collective excitations, the zero-sound modes. For attractive interactions, collective modes becomes damped as they mix with the particle-hole continuum. Notably, the pole acquires an imaginary component beyond a critical strength of the attractive interaction, which represents an instability in the particle-hole channel. The wave vector at which the instability is strongest gradually increases from 0 to nonzero wave vectors as the strength of the attractive interaction increases beyond the critical value. This indicates that the system becomes unstable against a density wave state in charge, spin, or bond for a strong attractive interaction (the schematic phase diagram is shown in Fig. 14 in Sec. V A).

In the particle-particle channel, poles of the coupling function capture the dynamics of collective modes with charge $2e$. Our finding is that the nontrivial dispersion of the Cooperon mode encoded in the momentum-dependent coupling function has an interesting dynamical consequence. When a superconducting condensate is nucleated within an unstable normal state subject to an attractive interaction, the system inevitably goes through a transient superconducting state in which the phase of the condensate is inhomogeneous in space (this can be inferred from the time evolution of the pair-pair correlation function shown in Fig. 16 in Sec. V B).

### A. Collective mode with charge 0: Density-density correlation function

Collective modes with zero charge and spin can be probed through the density-density correlation function. In terms of the Matsubara frequency, it is written as

$$\chi_{ph}(\vec{q}, i\omega_n) = \frac{1}{2}\sum_{\sigma,\sigma'}\int_0^\infty d\tau\ e^{i\omega_n\tau}\int\frac{d^2\vec{k}}{(2\pi)^2}\frac{d^2\vec{p}}{(2\pi)^2} \times\left\langle T_\tau \psi^\dagger_{\vec{k}+\frac{\vec{q}}{2},\sigma}(\tau)\psi_{\vec{k}-\frac{\vec{q}}{2},\sigma}(\tau)\psi^\dagger_{\vec{p}-\frac{\vec{q}}{2},\sigma'}(0)\psi_{\vec{p}+\frac{\vec{q}}{2},\sigma'}(0)\right\rangle. \quad (42)$$

It can be expressed as $\chi_{ph} = \chi_{ph}^{(0)} + \chi_{ph}^{(1)}$, where $\chi_{ph}^{(0)}(\vec{q}, i\omega_n) = \frac{k_F}{4\pi v_F}[1 - \frac{1}{\sqrt{1+\frac{v_F^2q^2}{\omega_n^2}}}]$ is the free-electron contribution and $\chi_{ph}^{(1)}$ is the interacting part. The interacting part is obtained by connecting the electron propagators to the one-particle irreducible quartic vertex function and summing over the relative momenta of particle-hole pairs as is shown

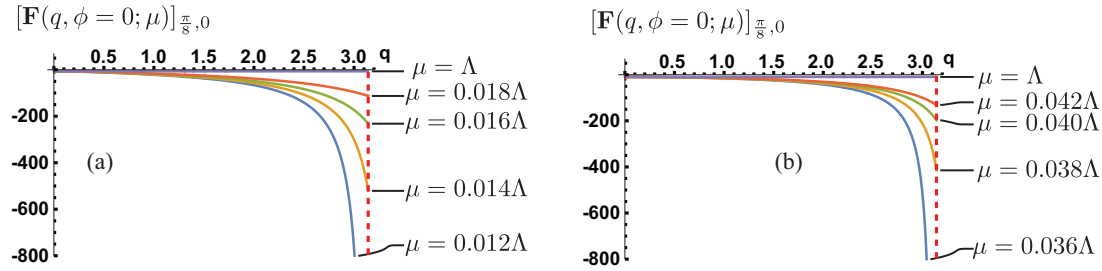


FIG. 7. RG flow of $[\mathbf{F}(q,\phi=0;\mu)]_{\frac{\pi}{8},0}$ for an attractive UV coupling function $[\mathbf{F}(q,\phi;\Lambda)]_{\theta,\theta'}=2\alpha\cos[2(\theta-\theta')]$ with (a) $\alpha=-(4\pi v_F+1)$ and (b) $\alpha=-(4\pi v_F+3)$. The coupling function diverges at the momentum cutoff $q_c=\pi$ at $\mu_c=0.122$ and $\mu_c=0.362$, respectively. We use $\Lambda=10$ and $v_F=0.3$.

below:

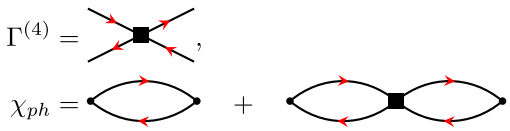


(43)

The nontrivial dynamics is encoded in the energy and momentum dependence of the vertex function. In our description, the coupling functions that depend on the momenta along the Fermi surface and the renormalization group energy scale contain that information through Eqs. (6) and (7). In the limit that the momentum carried by a particle-hole pair is small, the nearly-forward-scattering processes are most important. In this case, we can obtain the interacting part of the correlation function using our renormalized coupling function as

$$\chi^{(1)}_{ph}(\vec{q},i\omega_n)=-\frac{1}{2\beta^2}\sum_{\substack{\sigma,\sigma'\\ \sigma_1,\sigma_2,\sigma_3,\sigma_4}}\sum_{i\nu_n,i\nu_n'}\int\frac{d^2\vec{k}}{(2\pi)^2}\frac{d^2\vec{p}}{(2\pi)^2}\,G_\sigma\left(\vec{k}+\frac{\vec{q}}{2},i\omega_n+i\nu_n\right)G_\sigma\left(\vec{k}-\frac{\vec{q}}{2},i\nu_n\right)$$
$$\times\,\delta^\sigma_{\sigma_1}\delta^\sigma_{\sigma_4}\delta^{\sigma'}_{\sigma_2}\delta^{\sigma'}_{\sigma_3}(\lambda_0)^{\vec{k}+\frac{\vec{q}}{2},\sigma_1;\vec{p}-\frac{\vec{q}}{2},\sigma_2}_{\vec{k}-\frac{\vec{q}}{2},\sigma_4;\vec{p}+\frac{\vec{q}}{2},\sigma_3}G_{\sigma'}\left(\vec{p}+\frac{\vec{q}}{2},i\omega_n+i\nu_n'\right)G_{\sigma'}\left(\vec{p}-\frac{\vec{q}}{2},i\nu_n'\right)$$
$$=-\frac{k_F}{(4\pi v_F)^2}\int\frac{d\theta}{2\pi}\frac{d\theta'}{2\pi}\left[\frac{v_Fq\cos\theta}{-i\omega_n+v_Fq\cos\theta}\right][\mathbf{F}(q,\phi;\omega_n)]_{\theta,\theta'}\left[\frac{v_Fq\cos\theta'}{-i\omega_n+v_Fq\cos\theta'}\right]. \tag{44}$$

Below, we focus on the simplest case where the interaction is isotropic. For an interaction that is independent of angles at a UV scale $\Lambda$, the renormalized coupling function at energy scale $\mu$ is given by Eq. (25). In this case, the density-density correlation function is obtained to be

$$\chi_{ph}(\vec{q},i\omega_n)=\chi^{(0)}_{ph}(\vec{q},i\omega_n)+\chi^{(1)}_{ph}(\vec{q},i\omega_n)=\frac{k_F}{4\pi v_F}\left\{\frac{\alpha}{4\pi v_F}\left[\frac{1}{\sqrt{1+\frac{v_F^2q^2}{\Lambda^2}}}-1\right]+1\right\}\frac{\left[1-\frac{1}{\sqrt{1+\frac{v_F^2q^2}{\omega_n^2}}}\right]}{\frac{\alpha}{4\pi v_F}\left[\frac{1}{\sqrt{1+\frac{v_F^2q^2}{\Lambda^2}}}-\frac{1}{\sqrt{1+\frac{v_F^2q^2}{\omega_n^2}}}\right]+1}. \tag{45}$$

Notice that this observable exhibits a pole structure identical to the coupling function in Eq. (25) for an isotropic UV interaction. Therefore, analyzing these poles enables the study of excitations, including the particle-hole continuum and collective modes, without computing the specific observable explicitly. The retarded Green's function is obtained through the analytical continuation $i\omega_n\to\omega+i\delta$,

$$\chi_{ph}(\vec{q},\omega)=\frac{k_F}{4\pi v_F}\left\{\frac{\alpha}{4\pi v_F}\left[\frac{1}{\sqrt{1+\frac{v_F^2q^2}{\Lambda^2}}}-1\right]+1\right\}\frac{\left[1-\frac{1}{\sqrt{1-\frac{v_F^2q^2}{\omega^2}}}\right]}{\frac{\alpha}{4\pi v_F}\left[\frac{1}{\sqrt{1+\frac{v_F^2q^2}{\Lambda^2}}}-\frac{1}{\sqrt{1-\frac{v_F^2q^2}{\omega^2}}}\right]+1}. \tag{46}$$

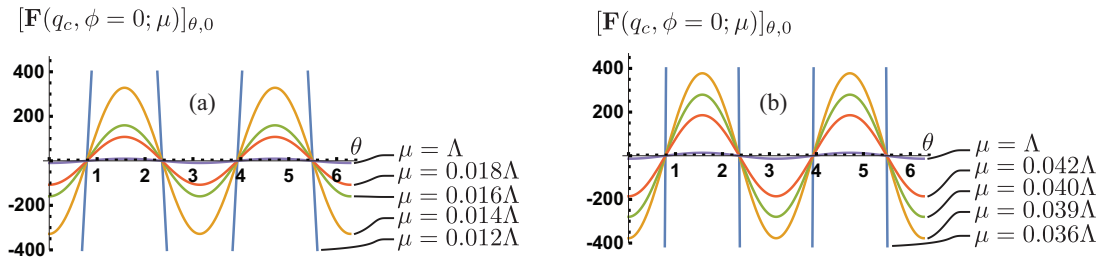


FIG. 8. $[\mathbf{F}(q, \phi = 0; \mu)]_{\theta,0}$ plotted as a function of $\theta$ at $q_c$ at different values of $\mu$ for (a) $\alpha = -(4\pi v_F + 1)$ and (b) $\alpha = -(4\pi v_F + 3)$. The critical energy scales correspond to $\mu_c = 0.122$ and $\mu_c = 0.362$, respectively. The same UV coupling function and parameters are used as in Fig. 7.

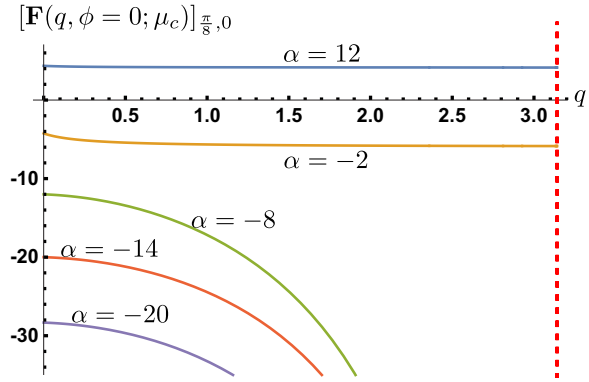


FIG. 9. The profile of the coupling function that emerges in the $\mu \to \mu_c$ limit from the UV coupling function $[\mathbf{F}(q, \phi; \Lambda)]_{\theta,\theta'} = 2\alpha \cos[2(\theta - \theta')]$ for different values of $\alpha$. $\mu_c = 0$ for stable Fermi liquids with $\alpha > -4\pi v_F \sqrt{1 + v_F^2 \frac{q^2}{\Lambda^2}}$. For unstable cases, the critical energy scales are given by $\mu_c = 0.491$, $\mu_c = 0.937$, and $\mu_c = 1.243$ for $\alpha = -8$, $\alpha = -14$, and $\alpha = -20$, respectively, for $v_F = 0.3$ and $\Lambda = 10$.

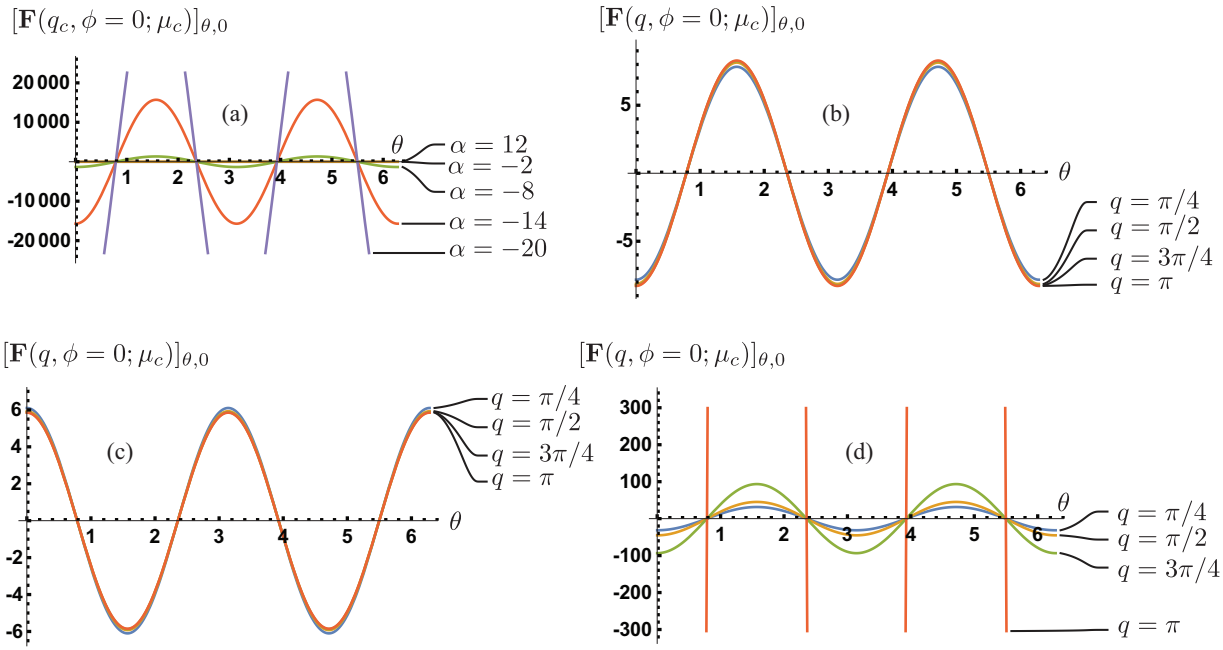


FIG. 10. The coupling function at the critical energy scale plotted as a function of $\theta$ and $q$ for the UV coupling function $[\mathbf{F}(q, \phi; \Lambda)]_{\theta,\theta'} = 2\alpha \cos[2(\theta - \theta')]$. (a) The coupling function at $\mu = \mu_c$ at $q = q_c$ for various choices of $\alpha$. (b) The coupling function at $\mu = 0$ for $\alpha = 12$. (c) The coupling function at $\mu = 0$ for $\alpha = -2$. (d) The coupling function at $\mu_c = 0.937$ for various choices of momenta for $\alpha = -14$. $\Lambda = 10$ and $v_F = 0.3$ are used for all plots.

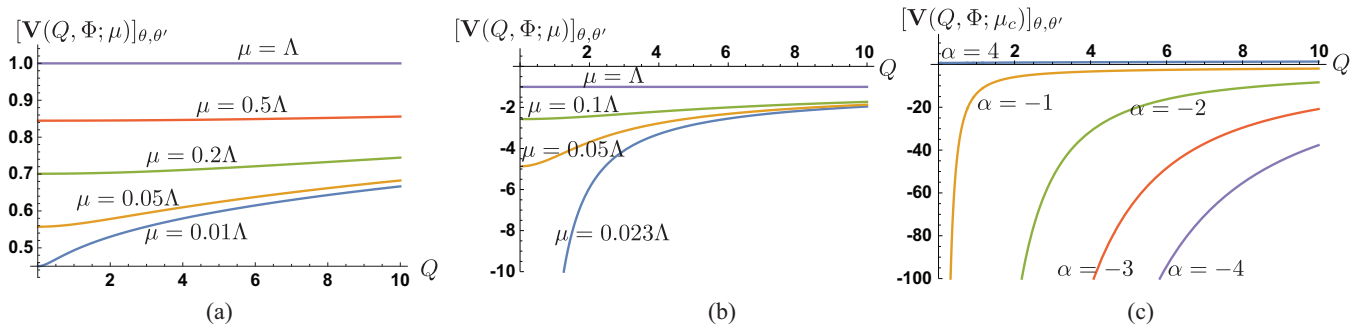


FIG. 11. The RG evolution of $[\mathbf{V}(Q,\phi;\mu)]_{\theta,\theta'}$ for the UV coupling in the $s$-wave channel with strength (a) $V_0(Q;\Lambda)=1$ and (b) $V_0(Q;\Lambda)=-1$ with $\mu_c=0.023$. (c) The coupling function that emerges in the $\mu\to\mu_c$ limit for different UV couplings. For repulsive UV couplings with $V_0(Q;\Lambda)>0$, the coupling function vanishes in the IR limit ($\mu_c=0$). For attractive couplings with $V_0(Q;\Lambda)=\alpha_V=-1,-2,-3,-4$, the pairing interaction $Q=0$ diverges at $\mu_c=0.23, 1.51, 2.84, 3.89$, respectively. We use $\Lambda=10$ and $v_F=0.3$.

Its imaginary part, which describes the spectral function for the neutral bosonic excitations, has a branch cut at $\omega=v_Fq$ associated with the particle-hole continuum,

$$\mathrm{Im}\chi_{ph}(\vec{q},\omega)=\begin{cases}\frac{k_F}{4\pi v_F}(\mathcal{A}-1)^2[\mathcal{A}^2-1]^{-\frac{3}{2}}\delta\left[\frac{\omega}{v_Fq}-\frac{\mathcal{A}}{\sqrt{\mathcal{A}^2-1}}\right] & \text{for } \omega>v_Fq \text{ and } \alpha>0\\ \frac{k_F}{4\pi v_F}(\mathcal{A}-1)^2\sqrt{\frac{v_F^2q^2}{\omega^2}-1}\left\{\mathcal{A}^2\left[\frac{v_F^2q^2}{\omega^2}-1\right]+1\right\}^{-1} & \text{for } \omega<v_Fq,\end{cases} \tag{47}$$

where $\mathcal{A}=\frac{4\pi v_F}{\alpha}+\frac{1}{\sqrt{1+\frac{v_F^2q^2}{\Lambda^2}}}$.

For a repulsive interaction ($\alpha>0$), the spectral function supports a delta-function peak outside the particle-hole continuum,

$$\frac{\omega}{v_Fq}=\frac{\mathcal{A}}{\sqrt{\mathcal{A}^2-1}}=\left[1+\frac{\alpha}{4\pi v_F}\frac{1}{\sqrt{1+\frac{v_F^2q^2}{\Lambda^2}}}\right]\left[\left(1+\frac{\alpha}{4\pi v_F}\frac{1}{\sqrt{1+\frac{v_F^2q^2}{\Lambda^2}}}\right)^2-\left(\frac{\alpha}{4\pi v_F}\right)^2\right]^{-\frac{1}{2}}. \tag{48}$$

In the $\Lambda\to\infty$ limit, the dispersion of the collective mode can be written in a closed form as $\frac{\omega}{v_Fq}=\frac{1+\frac{\alpha}{4\pi v_F}}{\sqrt{1+\frac{2\alpha}{4\pi v_F}}}$. This corresponds to the zero-sound mode. The spectral weight of the mode increases linearly in the forward-scattering amplitude in the weak-coupling limit. Besides the zero-sound mode, there also exists a broad peak inside the particle-hole continuum. The dispersion of the incoherent mode becomes

$$\frac{\omega}{v_Fq}=\frac{\left(1+\frac{\alpha}{4\pi v_F}\right)}{\sqrt{1+2\frac{\alpha}{4\pi v_F}\left(1+\frac{\alpha}{4\pi v_F}\right)}}<1 \tag{49}$$

in the $\Lambda\to\infty$ limit. In the strong-coupling limit, the velocity of this mode becomes $\frac{\omega}{v_Fq}=\frac{1}{\sqrt{2}}$. The height of the peak is $\mathrm{Max}[\mathrm{Im}\chi]=\frac{k_F}{4\pi v_F}\frac{1}{2(\frac{|\alpha|}{4\pi v_F})(1+\frac{\alpha}{4\pi v_F})}$, and the width at half maximum is given by

$$\frac{\Delta\omega}{v_Fq}=\sqrt{\frac{\left(1+\frac{\alpha}{4\pi v_F}\right)^2}{1+2\frac{\alpha}{4\pi v_F}+4(2-\sqrt{3})\left(\frac{\alpha}{4\pi v_F}\right)^2}}$$

$$-\sqrt{\frac{\left(1+\frac{\alpha}{4\pi v_F}\right)^2}{1+2\frac{\alpha}{4\pi v_F}+4(2+\sqrt{3})\left(\frac{\alpha}{4\pi v_F}\right)^2}}. \tag{50}$$

At weak coupling, the width scales with the coupling as $\Delta\omega\approx 4\sqrt{3}(\frac{\alpha}{4\pi v_F})^2v_Fq$. In the large $\alpha$ limit, the width becomes $\Delta\omega\approx\frac{1}{\sqrt{2}}v_Fq$. In the presence of an attractive interaction, the zero-sound mode is no longer sharply defined as the speed of the mode goes below the Fermi velocity, and the zero-sound mode merges with the incoherent mode [69]. The spectral function plotted as a function of $\omega/(v_Fq)$ is shown in Fig. 12 for different interaction strengths.

For sufficiently strong attractive interaction with $\alpha<\alpha_c=-4\pi v_F$, there exists a pole in the upper half plane of complex frequency at $\frac{\omega}{v_Fq}=i\frac{\mathcal{A}}{\sqrt{1-\mathcal{A}^2}}$. In the plane of $q$ and $\omega_n\equiv-i\omega$, the locations of the poles are shown for various values of the bare coupling in Fig. 13. At $\alpha=\alpha_c$, the spectral function exhibits a pole only at $q=0$ and $\omega_n=0$. In the channel in which the particle-hole pair carries spin 1, this corresponds to the Stoner instability associated with the ferromagnetic instability. For more general UV interactions, the instability can arise in channels with nonzero angular momenta in either the spin-singlet or spin-triplet channels associated with the Pomeranchuk instability. For

$\alpha < \alpha_c$, the spectral function exhibits a band of poles within $0 \leqslant \omega_n \leqslant \omega_{nc}(\alpha)$, where $\omega_{nc}(\alpha)$ corresponds to the largest imaginary frequency and the momentum associated with the pole is determined through $\frac{\alpha}{4\pi v_F} = \frac{-1}{\frac{1}{\sqrt{1+\frac{v_F^2 q^2}{\Lambda^2}}} - \frac{1}{\sqrt{1+\frac{v_F^2 q^2}{\omega_n^2}}}}$. If the imaginary frequency is lowered at a fixed $\alpha < \alpha_c$, the spectral function encounters the first pole at $\omega_{nc}(\alpha)$ with momentum

$$q_c(\alpha) = \Lambda \frac{\sqrt{2\sqrt{4\left(\frac{\alpha}{4\pi v_F}\right)^2 - 1}\left(\sqrt{4\left(\frac{\alpha}{4\pi v_F}\right)^2 - 1} - \sqrt{3}\right)}}{\left(\sqrt{4\left(\frac{\alpha}{4\pi v_F}\right)^2 - 1} + \sqrt{3}\right)} \quad \text{for } \alpha < \alpha_c. \tag{51}$$

The unstable modes with nonzero momenta correspond to density wave instabilities associated with charge, spin, or nematicity depending on the quantum number of the particle-hole pair. It is interesting to note that the strongest instability arises at $q \neq 0$ for $\alpha < \alpha_c$. $\omega_{nc}(\alpha)$ can be viewed as a rough estimate of the transition temperature of the spontaneous symmetry breaking triggered by the instability. In Fig. 14, we illustrate the phase diagram that indicates the transition temperature as a function of the interaction.

### B. Collective mode with charge 2: Pair-pair correlation function

The dynamics of charge 2 collective modes can be studied through the pair-pair correlation function. The correlation function in the $s$-wave channel reads

$$\begin{aligned}(\chi_{pp})^{\sigma_1,\sigma_2}_{\sigma_4,\sigma_3}(\vec{Q}, i\omega_n) &= \int_0^\infty d\tau\, e^{i\omega_n\tau} \int \frac{d^2\vec{k}}{(2\pi)^2}\frac{d^2\vec{k}'}{(2\pi)^2} \left\langle T_\tau \psi_{\vec{k}+\frac{\vec{Q}}{2},\sigma_4}(\tau)\psi_{-\vec{k}+\frac{\vec{Q}}{2},\sigma_3}(\tau)\psi^\dagger_{-\vec{k}'+\frac{\vec{Q}}{2},\sigma_2}(0)\psi^\dagger_{\vec{k}'+\frac{\vec{Q}}{2},\sigma_1}(0)\right\rangle \\ &= \int \frac{d^2\vec{k}}{(2\pi)^2}\frac{d^2\vec{k}'}{(2\pi)^2}\int^{\Lambda_\omega}\frac{d\omega'}{2\pi}\frac{d\Omega}{2\pi}\frac{d\Omega'}{2\pi}\left\langle \psi_{\vec{k}+\frac{\vec{Q}}{2},\sigma_4}(\omega_n-\omega')\psi_{-\vec{k}+\frac{\vec{Q}}{2},\sigma_3}(\omega')\psi^\dagger_{-\vec{k}'+\frac{\vec{Q}}{2},\sigma_2}(\Omega)\psi^\dagger_{\vec{k}'+\frac{\vec{Q}}{2},\sigma_1}(\Omega')\right\rangle, \end{aligned} \tag{52}$$

where $\vec{Q}$ and $\omega_n$ denote the center-of-mass momentum and energy of Cooper pairs. It can be written as $\chi_{pp} = \chi^{(0)}_{pp} + \chi^{(1)}_{pp}$, where $\chi^{(0)}_{pp}$ is the disconnected free-electron contribution and $(\chi^{(1)}_{pp})^{\sigma_1,\sigma_2}_{\sigma_4,\sigma_3}(\vec{Q}, i\omega_n)$ is the connected correlation function. For $\omega_n > 0$, the free-electron part is written as

$$\left(\chi^{(0)}_{pp}\right)^{\sigma_1,\sigma_2}_{\sigma_4,\sigma_3}(\vec{Q}, i\omega_n) = -\mathcal{A}^{\sigma_1,\sigma_2}_{\sigma_4,\sigma_3}\frac{k_F}{\pi v_F}\ln\frac{\omega_n}{4\Lambda_\omega}\left(1+\sqrt{1+\frac{v_F^2Q^2}{\omega_n^2}}\right), \tag{53}$$

where $\mathcal{A}^{\sigma_1,\sigma_2}_{\sigma_4,\sigma_3} = \frac{1}{2}(\delta^{\sigma_1}_{\sigma_4}\delta^{\sigma_2}_{\sigma_3} - \delta^{\sigma_1}_{\sigma_3}\delta^{\sigma_2}_{\sigma_4})$. Using Eqs. (6) and (7), one can express the connected correlation function in terms of the renormalized coupling function as

$$\begin{aligned}\left(\chi^{(1)}_{pp}\right)^{\sigma_1,\sigma_2}_{\sigma_4,\sigma_3}(\vec{Q}, i\omega_n) = &-\frac{1}{2}\int \frac{d^2\vec{k}_1}{(2\pi)^2}\frac{d^2\vec{k}_2}{(2\pi)^2}\left[(\lambda_1)^{\vec{k}_2+\frac{\vec{Q}}{2},\sigma_1;-\vec{k}_2+\frac{\vec{Q}}{2},\sigma_2}_{\vec{k}_1+\frac{\vec{Q}}{2},\sigma_4;-\vec{k}_1+\frac{\vec{Q}}{2},\sigma_3} - (\lambda_1)^{\vec{k}_2+\frac{\vec{Q}}{2},\sigma_1;-\vec{k}_2+\frac{\vec{Q}}{2},\sigma_2}_{-\vec{k}_1+\frac{\vec{Q}}{2},\sigma_3;\vec{k}_1+\frac{\vec{Q}}{2},\sigma_4}\right]\int^{\Lambda_\omega}\frac{d\omega'}{2\pi}\frac{d\Omega}{2\pi} \\ &\times G\left(\vec{k}_1+\frac{\vec{Q}}{2}, \omega_n-\omega'\right)G\left(-\vec{k}_1+\frac{\vec{Q}}{2}, \omega'\right)G\left(-\vec{k}_2+\frac{\vec{Q}}{2}, \Omega\right)G\left(\vec{k}_2+\frac{\vec{Q}}{2}, \omega_n-\Omega\right).\end{aligned} \tag{54}$$

Let us consider an isotropic UV interaction that is momentum independent: $V_0(Q, \Lambda) = \alpha_V$, where $\Lambda$ is the UV energy scale at which the bare coupling is defined. In this case, the connected correlation function becomes

$$\left(\chi^{(1)}_{pp}\right)^{\sigma_1,\sigma_2}_{\sigma_4,\sigma_3}(\vec{Q}, i\omega_n) = -\frac{1}{4k_F}\mathcal{A}^{\sigma_1,\sigma_2}_{\sigma_4,\sigma_3}V_0(Q;\omega_n)\left(\frac{k_F}{\pi v_F}\ln\left[\frac{\omega_n}{4\Lambda_\omega}\left(1+\sqrt{1+\frac{v_F^2Q^2}{\omega_n^2}}\right)\right]\right)^2, \tag{55}$$

where $\Lambda_\omega$ is the frequency cutoff. The precise value of the cutoff does not affect the low-energy physics. The correlation function in the spin-singlet channel can be singled out as $(\chi_{pp})^{\sigma_1,\sigma_2}_{\sigma_4,\sigma_3}(\vec{Q}, i\omega_n) = \mathcal{A}^{\sigma_1,\sigma_2}_{\sigma_4,\sigma_3}\chi^a_{pp}(\vec{Q}, i\omega_n)$, where

$$\chi^a_{pp}(\vec{Q}, i\omega_n) = \frac{k_F}{\pi v_F}\left[1+\frac{\alpha_V}{4\pi v_F}\ln\frac{\Lambda}{2\Lambda_\omega}\right]\frac{4\pi v_F}{\alpha_V} \times\left\{1+\frac{1+\frac{\alpha_V}{4\pi v_F}\ln\frac{\Lambda}{2\Lambda_\omega}}{\frac{\alpha_V}{4\pi v_F}\ln\frac{\sqrt{v_F^2Q^2+\omega_n^2}+\omega_n}{2\Lambda} - 1}\right\}. \tag{56}$$

To obtain the pair Green's function in real frequency, we use the analytic continuation and define $\chi^a_{pp}(\vec{Q}, \omega + i0^+)$. In the complex plane of $\omega$, $\chi^a_{pp}(\vec{Q}, \omega + i0^+)$ has a pole at $\omega = i\omega_Q$ with

$$\omega_Q = -e^{-\frac{4\pi v_F}{\alpha_V}}\frac{v_F^2Q^2}{4\Lambda} + e^{\frac{4\pi v_F}{\alpha_V}}\Lambda \tag{57}$$

and branch cuts slightly below the real axis with $|\omega| > v_FQ$. For a repulsive interaction ($\alpha_V > 0$), the pole and the branch cut are all in the lower half plane for any $Q \ll \Lambda/v_F$ [for $Q > \Lambda/v_F$, Eq. (56) is not valid]. For an attractive interaction ($\alpha_V < 0$), the pole lies in the upper half plane

for $Q < Q^*$, where $Q^* = \frac{2\Lambda}{v_F} e^{\frac{4\pi v_F}{\alpha_V}}$. This represents modes that grow exponentially in time associated with the superconducting instability. While all modes with center-of-mass momentum less than $Q^*$ become unstable, the $Q = 0$ mode exhibits the fastest growth (the largest imaginary frequency in the upper half plane).

Now, let us understand the dynamics of the unstable modes in more detail. To be concrete, we consider the following experimental setup. A metal, whose ground state is a superconductor with a small gap, is initially kept from becoming a superconductor by an external magnetic field. At $t = 0$, the magnetic field is turned off, and at the same time a superconducting tip is brought close to the system for a short period of time. The superconducting tip, which is a source of coherent Cooper pairs that can tunnel into the system, acts as a small pairing field $h_p$ applied to the system at $\vec{r} = 0$ and $t = 0$. This will trigger an avalanche of unstable modes, driving the system to the superconducting ground state. With other superconducting tips that are located at finite distances away from the initial superconducting tip, one can probe the spatial and temporal profile that arises from the real-time evolution of the

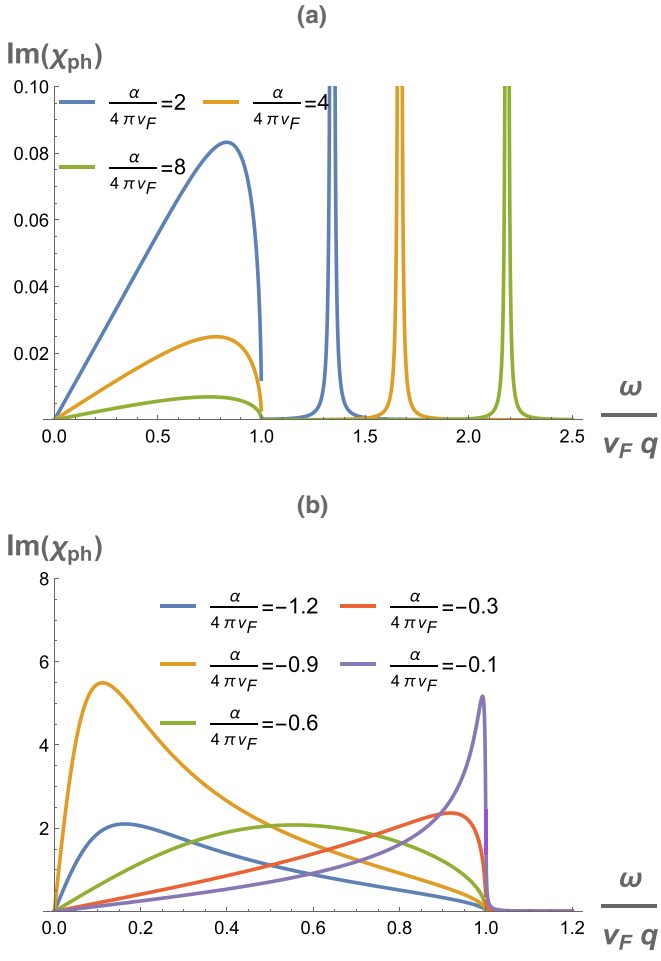


FIG. 12. $\mathrm{Im}\chi_{ph}(\vec{q}, \omega)$ as a function of $\frac{\omega}{v_F q}$ (horizontal axis) at various (a) positive $\frac{\alpha}{4\pi v_F}$ and (b) negative $\frac{\alpha}{4\pi v_F}$. The zero-sound modes correspond to the sharp peaks at $\frac{\omega}{v_F q} \gtrsim 1$. The damped modes correspond to the broad peaks at $\frac{\omega}{v_F q} < 1$. $\Lambda = 40$ and $\delta = 0.0001$

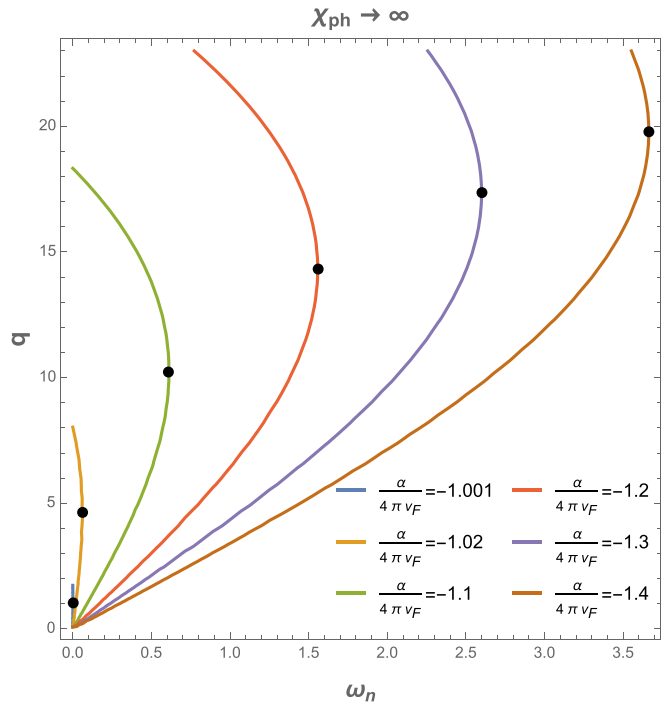


FIG. 13. The location of poles in the particle-hole spectral function as a function of $q$ and $\omega_n \equiv -i\omega$ for different choices of $\frac{\alpha}{4\pi v_F}$, where $\alpha$ denotes the bare interaction in the $s$-wave channel that is momentum independent at energy scale $\Lambda = 40$. Black dots represent $(\omega_{nc}(\alpha), q_c(\alpha))$ that correspond to the pole with the largest imaginary frequency at each $\alpha$.

condensate. Within the period of the initial growth when the amplitude of the pair condensate is small, the linear response theory is valid, and the condensate of momentum $\vec{Q}$ at time $t$ is written as

$$P(\vec{Q}, t) = h_p \mathcal{G}_{pp}(\vec{Q}, t), \tag{58}$$

where $h_p$ is the pairing field applied at $t = 0$ and $\vec{r} = 0$ and $\mathcal{G}_{pp}(\vec{Q}, t)$ is the regarded Green's function that satisfies the boundary condition $\mathcal{G}_{pp}(\vec{Q}, t) = 0$ for $t < 0$.

However, $\chi^a_{pp}(\vec{Q}, \omega + i0^+)$ itself does not give the retarded Green's function because it has poles in the upper half plane. The Fourier transformation of $\chi^a_{pp}(\vec{Q}, \omega + i0^+)$ along the real axis of $\omega$ gives

$$G_{pp}(\vec{Q}, t) = \Theta(-t)\mathcal{G}^{(0)}_{pp}(\vec{Q}, t) + \Theta(t)\mathcal{G}^{(1)}_{pp}(\vec{Q}, t), \tag{59}$$

where

$$\mathcal{G}^{(0)}_{pp}(\vec{Q}, t) = -\frac{k_F}{\pi v_F}\left(\frac{4\pi v_F}{\alpha_V}\right)^2 \Theta(Q^* - |\vec{Q}|) e^{\omega_Q t} \times \left[e^{-\frac{4\pi v_F}{\alpha_V}} \frac{v_F^2 Q^2}{4\Lambda} + e^{\frac{4\pi v_F}{\alpha_V}} \Lambda\right],$$
$$\mathcal{G}^{(1)}_{pp}(\vec{Q}, t) = \int \frac{d\omega}{2\pi} e^{-i\omega t} \chi^a_{pp}(\vec{Q}, \omega + i\eta). \tag{60}$$

$\mathcal{G}^{(0)}_{pp}(\vec{Q}, t)$ is the contribution of the pole located in the upper half plane for $Q < Q^*$, which can be picked up by extending the frequency integration of $\chi^a_{pp}(\vec{Q}, \omega + i\eta)$ along the real axis with the infinite semicircle in the upper half plane at $t < 0$.

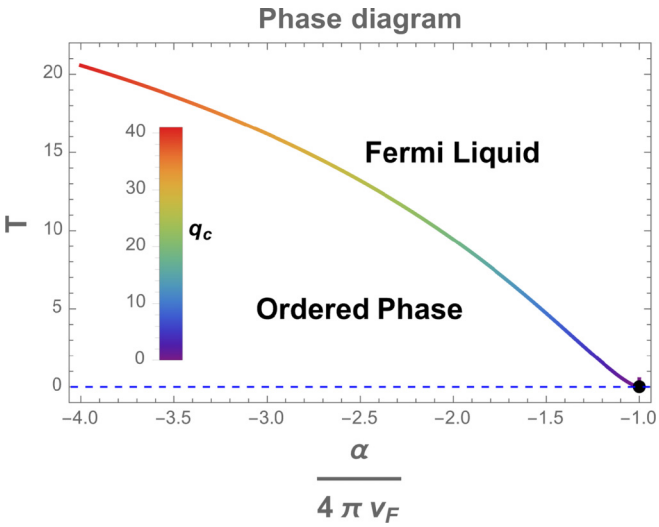


FIG. 14. Phase diagram of the two-dimensional Fermi liquids in the plane of bare interaction $\alpha$ and temperature $T$ suggested from the one-loop renormalized coupling function. Here, we use $\omega_{nc}(\alpha)$ as the proxy for the transition temperature. The regions above and below the curve represent the symmetric Fermi liquid and a symmetry-broken state, respectively. The color changing along the phase boundary represents evolution of the ordering wave vector, $q_c(\alpha)$. As $\alpha$ decreases below $\alpha_c$, $q_c(\alpha)$ gradually increases from zero following Eq. (51). The black dot at $(-1.0, 0.0)$ denotes the uniform Stoner instability.

The hard cutoff $Q^*$ for the momentum integration reflects the fact that the Cooper pair mode is unstable only for $Q < Q^*$. $\mathcal{G}^{(1)}_{pp}(\vec{Q}, t)$ represents the contributions of the poles in the lower half plane.

$G_{pp}(\vec{Q}, t)$ is nonzero at all $t$ and decays exponentially in the $|t| \to \infty$ limit because $\mathcal{G}^{(0)}_{pp}(\vec{Q}, t)$ and $\mathcal{G}^{(1)}_{pp}(\vec{Q}, t)$ decay at large negative and positive $t$, respectively, as is shown in Fig. 15. What Eq. (59) describes is the evolution of a pair condensate that existed even before the pair field is applied at $t = 0$, where its amplitude gradually increases from zero to a finite value as $t$ increases from $-\infty$ to 0. While the condensate would have kept growing in $t > 0$, the field applied at $t = 0$

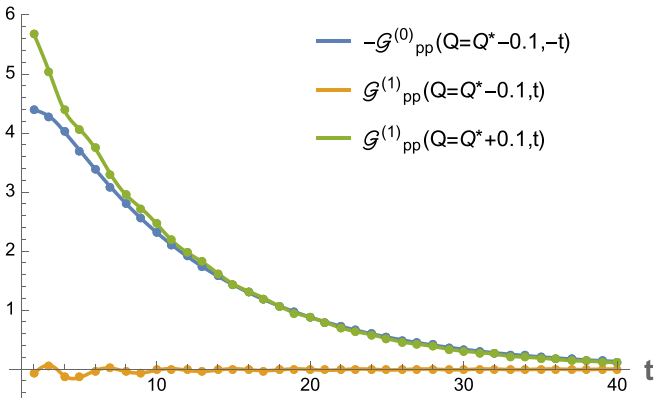


FIG. 15. $-\mathcal{G}^{(0)}_{pp}(\vec{Q}^* - 0.1, -t)$ and $\mathcal{G}^{(1)}_{pp}(\vec{Q}^* \pm 0.1, t)$ plotted as a function of $t > 0$ for $\eta = 0.001$, $\Lambda = 6$, $\Lambda_\omega = 100$, and $\frac{\alpha_V}{4\pi v_F} = -0.5$. $\mathcal{G}^{(1)}_{pp}(\vec{Q}, t)$ has been numerically evaluated with $m = \frac{k_F}{v_F} = \pi$ and $v_F = 1$.

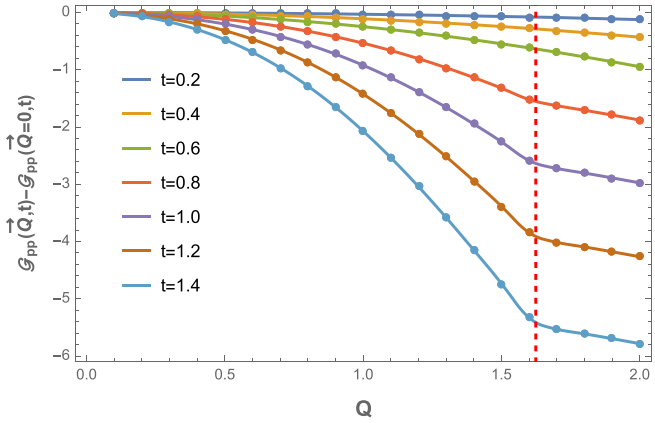


FIG. 16. $\mathcal{G}_{pp}(\vec{Q}, t) - \mathcal{G}_{pp}(0, t)$ plotted as a function of $Q$ for $0.2 \leqslant t \leqslant 1.4$ with $\eta = 0.001$, $\Lambda = 6$, $\frac{\alpha_V}{4\pi v_F} = -0.5$, and $\Lambda_\omega = 100$. The red dashed line denotes the location of $Q^*$.

alters the condensate into $\mathcal{G}^{(1)}_{pp}(\vec{r}, t)$ in $t > 0$ [70]. To describe the situation in which the condensate amplitude is zero in $t < 0$, one has to add a time-dependent condensate that exists without the external source and cancels Eq. (59) in $t < 0$. Therefore the retarded Green's function becomes

$$\mathcal{G}_{pp}(\vec{Q}, t) = G_{pp}(\vec{Q}, t) - \mathcal{G}^{(0)}_{pp}(\vec{Q}, t). \tag{61}$$

Equation (61) satisfies the desired boundary condition, $\mathcal{G}_{pp}(\vec{Q}, t < 0) = 0$. Furthermore, $\mathcal{G}^{(0)}_{pp}(\vec{Q}, t)$ now captures the exponentially growing condensate in $t > 0$.

We plot $\mathcal{G}_{pp}(\vec{Q}, t)$ as a function of $Q$ in Fig. 16. In the small $t$ limit, $\mathcal{G}_{pp}(Q, t)$ is independent of $Q$. This gives a delta function in real space, which describes a localized pair condensate created by the local pair field applied at $t = 0$. With increasing $t$, $\mathcal{G}_{pp}(Q, t)$ develops a nontrivial profile as condensates with different momenta grow at different rates. The mode with $Q = 0$ grows at the fastest rate, but all modes with $Q < Q^*$ grow independently as long as the amplitude of the condensate is small enough that the interaction between Cooper pairs can be ignored. This gives rise to a spatial inhomogeneity in the phase of the condensate. To see this, we consider $t \gg \Lambda/(v_F Q^*)^2$ but small enough that the amplitude of condensate is small. In this case, $\mathcal{G}^{(0)}_{pp}(\vec{Q}, t)$ gives the dominant contribution, and the Green's function is well approximated by

$$\begin{aligned}\mathcal{G}_{pp}(\vec{r}, t) &\approx -\mathcal{G}^{(0)}_{pp}(\vec{r}, t) \\ &= \frac{k_F}{\pi v_F}\frac{v_F Q^*}{2\pi}\left(\frac{4\pi v_F}{\alpha_V}\right)^2 \\ &\quad \times \frac{v_F^2 t(2 + v_F Q^* t) - v_F Q^* r^2}{2v_F^2 t^3} e^{-\frac{v_F Q^* r^2}{2v_F^2 t} + \frac{v_F Q^*}{2} t}.\end{aligned} \tag{62}$$

Equation (62) describes a diffusive behavior of the exponentially growing pair condensate. It is interesting to note that $\mathcal{G}^{(0)}_{pp}(\vec{r}, t)$ is positive for $r < r_c$ with $r_c = \sqrt{\frac{v_F t(2+v_F Q^* t)}{Q^*}}$ while it becomes negative for $r > r_c$. At $r_{\min} = \sqrt{\frac{v_F t(4+v_F Q^* t)}{Q^*}}$, the condensate becomes most negative, and its magnitude

decreases algebraically in $t$: $\mathcal{G}^{(0)}_{pp}(\vec{r}_{\min}, t) = -\frac{k_F}{\pi v_F}(\frac{4\pi v_F}{\alpha_V})^2 \frac{v_F Q^*}{2\pi e^2 t^2}$. The inclusion of $\mathcal{G}^{(1)}_{pp}(\vec{r}_{\min}, t)$, which is exponentially small at large $t$, will modify the precise location of $r_c$ but will not remove the region of the condensate with phase difference $\pi$. The appearance of the inverted condensate in $r > r_c$ is a consequence of the unstable modes with nonzero momenta. The exponentially growing modes with nonzero $Q$ cause a destructive interference at $r_c$ and the inverted condensate in $r > r_c$. With increasing time, the in-phase condensate near $\vec{r} = 0$ pushes the inverted condensate to the region outside radius $r_c \sim v_F t$ as the modes with nonzero $Q$ grow more slowly than the uniform condensate. In the ultimate long-time limit, the interaction between Cooper pairs kicks in to stabilize the uniform superconducting state. However, the appearance of the transient superconducting condensate with phase shift $\pi$ is unavoidable in the initial time period when the amplitude of the condensate is still small.

The results discussed in this section can in principle be obtained by computing the density-density and pair-pair correlation functions directly from a microscopic model that includes short-ranged interactions. Then, what is the merit of using this low-energy effective theory? First, our local effective field theory keeps all universal information and explains low-energy phenomena such as the collective modes in a self-contained manner. This is in contrast to Landau's fixed-point theory, which cannot describe the collective modes without including certain "high-energy" information which is not part of the fixed-point theory [71]. Second, the effective field theory makes the universal nature of physical predictions manifest. The relations between low-energy observables that are determined from the fixed-point coupling functions are guaranteed to be universal because the coupling functions depend only on the universal low-energy data of the fixed point. Finally, the present framework of local low-energy effective field theory can be readily generalized to non-Fermi liquids for which critical nonforward scatterings play even more important roles than in Fermi liquids [61].

In this paper, we considered neutral Fermi liquids. For charged Fermi liquids, the long-range Coulomb interaction is expected to qualitatively modify the functional renormalization group flow and the nature of the collective modes. However, the theoretical formalism developed in this paper can be readily applied to charged Fermi liquids. We defer the full discussion of the charged Fermi liquid to a follow-up paper.

## VI. SUMMARY

In summary, we study the Landau Fermi liquid and its instabilities within the low-energy effective field theory that is valid beyond the strict zero-energy limit. The local effective field theory should include general coupling functions that include nonforward scatterings and pairing interactions with nonzero center-of-mass momenta. At low energies, the coupling functions exhibit universal scaling behaviors when the momentum transfer and the center-of-mass momentum are comparable to the energy scale. The scaling behavior of the general coupling functions determines various physical observables at low energies [11–13,72]. In particular, the dynamics of the low-energy collective modes is fully encoded within the momentum-dependent coupling functions. This allows us to understand all low-energy physics of Fermi liquids within the low-energy effective field theory without resorting to microscopic theories. We reproduce universal dynamics of the zero-sound mode from the momentum-dependent coupling function in the particle-hole channel. The coupling functions also contain the dynamical information about the unstable modes in the presence of instabilities. As an unstable normal Fermi liquid evolves toward the superconducting ground state, we predict that it inevitably goes through a period of inhomogeneous superconductivity with a local phase inversion in the superconducting condensate due to the universal momentum dependence of the renormalized coupling function in the particle-particle channel. The local low-energy effective field theory valid away from the strict zero-energy limit also reveals alternative types of instabilities of Fermi liquids. Unlike the forward-scattering amplitude, which is exactly marginal, the nonforward-scattering amplitudes are subject to nontrivial quantum corrections. If the strength of the bare attractive interaction exceeds a critical strength, it can drive instabilities toward symmetry-broken states in particle-hole channels. The momentum-dependent coupling functions can also be tested more directly through double photoemission spectroscopy [73].

## ACKNOWLEDGMENTS

We thank R. Shankar for a discussion. Research at the Perimeter Institute is supported in part by the Government of Canada through Industry Canada and by the Province of Ontario through the Ministry of Research and Information. S.-S.L. also acknowledges support from the Natural Sciences and Engineering Research Council of Canada.

[1] L. Landau, The theory of a Fermi liquid, Sov. Phys. JETP **3**, 920 (1957).

[2] L. Landau, On the theory of the Fermi liquid, Sov. Phys. JETP **8**, 70 (1959).

[3] A. A. Abrikosov, L. P. Gorkov, and I. E. Dzyaloshinski, *Methods of Quantum Field Theory in Statistical Physics* (Courier, New York, 2012).

[4] D. Pines and P. Nozières, Microscopic theories of the electron liquid, in *Theory of Quantum Liquids* (CRC, Boca Raton, FL, 2018), pp. 270–344.

[5] A. A. Abrikosov and I. M. Khalatnikov, Theory of Fermi liquid. Properties of liquid $He^3$ at low temperatures, Usp. Fiz. Nauk **66**, 177 (1958).

[6] P. Nozières and J. M. Luttinger, Derivation of the Landau theory of Fermi liquids. I. Formal preliminaries, Phys. Rev. **127**, 1423 (1962).

[7] J. M. Luttinger and P. Nozières, Derivation of the Landau theory of fermi liquids. II. Equilibrium properties and transport equation, Phys. Rev. **127**, 1431 (1962).

[8] R. Shankar, Renormalization-group approach to interacting fermions, Rev. Mod. Phys. **66**, 129 (1994).

[9] J. Polchinski, Effective field theory and the Fermi surface, arXiv:hep-th/9210046.

[10] G. Benfatto and G. Gallavotti, Renormalization-group approach to the theory of the Fermi surface, Phys. Rev. B **42**, 9967 (1990).

[11] A. V. Chubukov, D. L. Maslov, and A. J. Millis, Nonanalytic corrections to the specific heat of a three-dimensional Fermi liquid, Phys. Rev. B **73**, 045128 (2006).

[12] A. V. Chubukov and D. L. Maslov, Singular corrections to the Fermi-liquid theory, Phys. Rev. B **69**, 121102(R) (2004).

[13] H. K. Pal, V. I. Yudson, and D. L. Maslov, Resistivity of non-Galilean-invariant Fermi- and non-Fermi liquids, Lith. J. Phys. **52**, 142 (2012).

[14] S. Das Sarma and Y. Liao, Know the enemy: 2D Fermi liquids, Ann. Phys. (Amsterdam) **435**, 168495 (2021).

[15] T. Holstein, R. E. Norton, and P. Pincus, de Haas-van Alphen effect and the specific heat of an electron gas, Phys. Rev. B **8**, 2649 (1973).

[16] J. A. Hertz, Quantum critical phenomena, Phys. Rev. B **14**, 1165 (1976).

[17] P. A. Lee, Gauge field, Aharonov-Bohm flux, and high-$T_c$ superconductivity, Phys. Rev. Lett. **63**, 680 (1989).

[18] M. Y. Reizer, Relativistic effects in the electron density of states, specific heat, and the electron spectrum of normal metals, Phys. Rev. B **40**, 11571 (1989).

[19] P. A. Lee and N. Nagaosa, Gauge theory of the normal state of high-$T_c$ superconductors, Phys. Rev. B **46**, 5621 (1992).

[20] C. M. Varma, P. B. Littlewood, S. Schmitt-Rink, E. Abrahams, and A. E. Ruckenstein, Phenomenology of the normal state of Cu-O high-temperature superconductors, Phys. Rev. Lett. **63**, 1996 (1989).

[21] A. J. Millis, Effect of a nonzero temperature on quantum critical points in itinerant fermion systems, Phys. Rev. B **48**, 7183 (1993).

[22] B. L. Altshuler, L. B. Ioffe, and A. J. Millis, Low-energy properties of fermions with singular interactions, Phys. Rev. B **50**, 14048 (1994).

[23] Y. B. Kim, A. Furusaki, X.-G. Wen, and P. A. Lee, Gauge-invariant response functions of fermions coupled to a gauge field, Phys. Rev. B **50**, 17917 (1994).

[24] C. Nayak and F. Wilczek, Non-Fermi liquid fixed point in 2 + 1 dimensions, Nucl. Phys. B **417**, 359 (1994).

[25] J. Polchinski, Low-energy dynamics of the spinon-gauge system, Nucl. Phys. B **422**, 617 (1994).

[26] A. Abanov and A. V. Chubukov, Spin-fermion model near the quantum critical point: One-loop renormalization group results, Phys. Rev. Lett. **84**, 5608 (2000).

[27] A. Abanov, A. V. Chubukov, and J. Schmalian, Quantum-critical theory of the spin-fermion model and its application to cuprates: Normal state analysis, Adv. Phys. **52**, 119 (2003).

[28] A. Abanov and A. Chubukov, Anomalous scaling at the quantum critical point in itinerant antiferromagnets, Phys. Rev. Lett. **93**, 255702 (2004).

[29] H. v. Löhneysen, A. Rosch, M. Vojta, and P. Wölfle, Fermi-liquid instabilities at magnetic quantum phase transitions, Rev. Mod. Phys. **79**, 1015 (2007).

[30] T. Senthil, Critical Fermi surfaces and non-Fermi liquid metals, Phys. Rev. B **78**, 035103 (2008).

[31] S.-S. Lee, Low-energy effective theory of Fermi surface coupled with U(1) gauge field in 2 + 1 dimensions, Phys. Rev. B **80**, 165102 (2009).

[32] D. F. Mross, J. McGreevy, H. Liu, and T. Senthil, Controlled expansion for certain non-Fermi-liquid metals, Phys. Rev. B **82**, 045121 (2010).

[33] M. A. Metlitski and S. Sachdev, Quantum phase transitions of metals in two spatial dimensions. I. Ising-nematic order, Phys. Rev. B **82**, 075127 (2010).

[34] M. A. Metlitski and S. Sachdev, Quantum phase transitions of metals in two spatial dimensions. II. Spin density wave order, Phys. Rev. B **82**, 075128 (2010).

[35] S. A. Hartnoll, D. M. Hofman, M. A. Metlitski, and S. Sachdev, Quantum critical response at the onset of spin-density-wave order in two-dimensional metals, Phys. Rev. B **84**, 125115 (2011).

[36] E. Abrahams and P. Wölfe, Critical quasiparticle theory applied to heavy fermion metals near an antiferromagnetic quantum phase transition, Proc. Natl. Acad. Sci. USA **109**, 3238 (2012).

[37] H.-C. Jiang, M. S. Brock, R. V. Mishmash, J. R. Garrison, D. Sheng, O. I. Motrunich, and M. P. Fisher, Non-Fermi-liquid $d$-wave metal phase of strongly interacting electrons, Nature (London) **493**, 39 (2013).

[38] A. L. Fitzpatrick, S. Kachru, J. Kaplan, and S. Raghu, Non-Fermi-liquid fixed point in a Wilsonian theory of quantum critical metals, Phys. Rev. B **88**, 125116 (2013).

[39] D. Dalidovich and S.-S. Lee, Perturbative non-Fermi liquids from dimensional regularization, Phys. Rev. B **88**, 245106 (2013).

[40] P. Strack and P. Jakubczyk, Fluctuations of imbalanced fermionic superfluids in two dimensions induce continuous quantum phase transitions and non-Fermi-liquid behavior, Phys. Rev. X **4**, 021012 (2014).

[41] S. Sur and S.-S. Lee, Chiral non-Fermi liquids, Phys. Rev. B **90**, 045121 (2014).

[42] A. A. Patel and S. Sachdev, dc resistivity at the onset of spin density wave order in two-dimensional metals, Phys. Rev. B **90**, 165146 (2014).

[43] S. Sur and S.-S. Lee, Quasilocal strange metal, Phys. Rev. B **91**, 125136 (2015).

[44] S. P. Ridgway and C. A. Hooley, Non-Fermi-liquid behavior and anomalous suppression of Landau damping in layered metals close to ferromagnetism, Phys. Rev. Lett. **114**, 226404 (2015).

[45] T. Holder and W. Metzner, Anomalous dynamical scaling from nematic and U(1) gauge field fluctuations in two-dimensional metals, Phys. Rev. B **92**, 041112(R) (2015).

[46] A. A. Patel, P. Strack, and S. Sachdev, Hyperscaling at the spin density wave quantum critical point in two-dimensional metals, Phys. Rev. B **92**, 165105 (2015).

[47] C. M. Varma, Quantum criticality in quasi-two-dimensional itinerant antiferromagnets, Phys. Rev. Lett. **115**, 186405 (2015).

[48] A. Eberlein, Self-energy effects in functional renormalization group flows of the two-dimensional $t-t'$ Hubbard model away from van Hove filling, Phys. Rev. B **92**, 235146 (2015).

[49] Y. Schattner, S. Lederer, S. A. Kivelson, and E. Berg, Ising nematic quantum critical point in a metal: A Monte Carlo study, Phys. Rev. X **6**, 031028 (2016).

[50] S. Sur and S.-S. Lee, Anisotropic non-Fermi liquids, Phys. Rev. B **94**, 195135 (2016).

[51] D. Chowdhury, Y. Werman, E. Berg, and T. Senthil, Translationally invariant non-Fermi-liquid metals with critical Fermi surfaces: Solvable models, Phys. Rev. X **8**, 031024 (2018).

[52] C. M. Varma, W. J. Gannon, M. C. Aronson, J. A. Rodriguez-Rivera, and Y. Qiu, Quantum critical singularities in two-dimensional metallic XY ferromagnets, Phys. Rev. B **97**, 085134 (2018).

[53] W. Ye, S.-S. Lee, and L. Zou, Ultraviolet-infrared mixing in marginal Fermi liquids, Phys. Rev. Lett. **128**, 106402 (2022).

[54] S.-S. Lee, Recent developments in non-Fermi liquid theory, Annu. Rev. Condens. Matter Phys. **9**, 227 (2018).

[55] D. V. Else, R. Thorngren, and T. Senthil, Non-Fermi liquids as ersatz Fermi liquids: General constraints on compressible metals, Phys. Rev. X **11**, 021005 (2021).

[56] Z. D. Shi, H. Goldman, D. V. Else, and T. Senthil, Gifts from anomalies: Exact results for Landau phase transitions in metals, SciPost Phys. **13**, 102 (2022).

[57] D. Khveshchenko, Novel approaches to generic non-Fermi liquids: higher-dimensional bosonization vs generalized holography, Lith. J. Phys. **63**, 85 (2023).

[58] A. H. Castro Neto and E. Fradkin, Bosonization of Fermi liquids, Phys. Rev. B **49**, 10877 (1994).

[59] A. Houghton, H.-J. Kwon, and J. B. Marston, Multidimensional bosonization, Adv. Phys. **49**, 141 (2000).

[60] L. V. Delacretaz, Y.-H. Du, U. Mehta, and D. T. Son, Nonlinear bosonization of Fermi surfaces: The method of coadjoint orbits, Phys. Rev. Res. **4**, 033131 (2022).

[61] F. Borges, A. Borissov, A. Singh, A. Schlief, and S.-S. Lee, Field-theoretic functional renormalization group formalism for non-Fermi liquids and its application to the antiferromagnetic quantum critical metal in two dimensions, Ann. Phys. (Amsterdam) **450**, 169221 (2023).

[62] It is noted that both $\lambda_0$ and $\lambda_1$ include the process in which two fermions with almost zero center-of-mass momentum go through a near-forward scattering. However, the phase space for such overlap is a set of measure zero in the low-energy limit.

[63] Alternatively, one can adopt a scaling in which the angle is rescaled with a fixed $k_F$ [74].

[64] The action that includes higher-order interactions also has dimension 1 under the current scale transformation. However, we do not include them here as they do not give rise to IR singularities [61].

[65] S.-W. Tsai, A. H. Castro Neto, R. Shankar, and D. K. Campbell, Renormalization-group approach to strong-coupled superconductors, Phys. Rev. B **72**, 054531 (2005).

[66] Here we have

$$d\bar{\mathcal{V}}_{2;B} = d\omega_B d\kappa d\theta,$$
$$d\bar{\mathcal{V}}^{(0)}_{4;B} = d\omega_B d\Omega_B d\Omega'_B d\kappa d\rho d\phi d q q d\theta d\theta',$$
$$d\bar{\mathcal{V}}^{(1)}_{4;B} = d\omega_B d\Omega_B d\Omega'_B d\kappa d\rho d\Phi d Q Q d\theta d\theta',$$
$$\vartheta^S_{\theta,B} = \frac{q}{2k_{F;B}}\sin(\theta-\phi), \quad \varphi^S_{\theta,B} = \frac{Q}{2k_{F;B}}\sin(\theta-\Phi),$$
$$\vartheta^C_{\theta,B} = \frac{q}{2k_{F;B}}\cos(\theta-\phi), \quad \varphi^C_{\theta,B} = \frac{Q}{2k_{F;B}}\cos(\theta-\Phi).$$

.

[67] If the UV coupling is weak, we can write down the fixed-point coupling function in powers of the UV coupling function as $[\tilde{\mathbf{F}}(\tilde{q},\phi;\mu)]_{\theta,\theta'} = [\mathbf{F}(0,\phi;\infty)]_{\theta,\theta'} - \frac{1}{8\pi^2 v_F}\int_0^{2\pi} d\Theta\, [\mathbf{F}(0,\phi;\infty)]_{\theta,\Theta}\frac{v_F^2\tilde{q}^2\cos^2(\Theta-\phi)}{1+v_F^2\tilde{q}^2\cos^2(\Theta-\phi)}[\mathbf{F}(0,\phi;\infty)]_{\Theta,\theta'} + \cdots$.

[68] B. Spivak and S. A. Kivelson, Phases intermediate between a two-dimensional electron liquid and Wigner crystal, Phys. Rev. B **70**, 155114 (2004).

[69] The modes at $-\frac{1}{2}<\alpha<0$ are referred to as hidden modes [75,76].

[70] This is analogous to the situation where a ball slowly rolls down from the top of a mountain before it is kicked back so that it climbs back to the top in the $t \to \infty$ limit.

[71] For example, in Landau's kinetic theory, the energy functional $E = \int dx d\theta d\theta'\, F(\theta,\theta') f(x,\theta) f(x,\theta')$ is used to describe the collective modes of the Fermi surface, where $f(x,\theta)$ describes the position-dependent displacement of the Fermi surface at angle $\theta$ and $F(\theta,\theta')$ is the Landau function. However, this energy function actually includes the nonforward scattering that is independent of momentum transfer.

[72] A. V. Chubukov and D. L. Maslov, First-Matsubara-frequency rule in a Fermi liquid. I. Fermionic self-energy, Phys. Rev. B **86**, 155136 (2012).

[73] R. Herrmann, S. Samarin, H. Schwabe, and J. Kirschner, Two electron photoemission in solids, Phys. Rev. Lett. **81**, 2148 (1998).

[74] S.-S. Lee, Stability of the U(1) spin liquid with a spinon Fermi surface in $2+1$ dimensions, Phys. Rev. B **78**, 085129 (2008).

[75] A. Klein, D. L. Maslov, L. P. Pitaevskii, and A. V. Chubukov, Collective modes near a Pomeranchuk instability in two dimensions, Phys. Rev. Res. **1**, 033134 (2019).

[76] A. Klein, D. L. Maslov, and A. V. Chubukov, Hidden and mirage collective modes in two dimensional Fermi liquids, npj Quantum Mater. **5**, 55 (2020).